UNIVERSITY OF HELSINKI REPORT SERIES IN PHYSICS

HU-P-D220

# CHARACTERIZATION OF SYNCHROTRON RADIATION BASED FUNCTIONAL LUNG IMAGING

**Satu Strengell**

Division of Material Physics
Department of Physics
Faculty of Science
and
Department of Clinical Physiology
and Nuclear Medicine
HUS Medical Imaging Center
Helsinki University Central Hospital
University of Helsinki
Helsinki, Finland

*ACADEMIC DISSERTATION*

*To be presented, with the permission of*
*the Faculty of Science of the University of Helsinki,*
*for public criticism in Auditorium 107 of Athena,*
*Siltavuorenpenger 3A,*
*on October 10st, 2014, at 12 o'clock.*

Helsinki 2014

**Supervisors:**

Professor Anssi Sovijärvi
Department of Clinical Physiology
and Nuclear Medicine
HUS Medical Imaging Center
Helsinki University Central Hospital
University of Helsinki
Finland

Docent Liisa Porra
Division of Material Physics
Department of Physics
Faculty of Science
University of Helsinki
Finland

**Pre-examiners:**

Professor Per Wollmer
Department of Clinical Sciences
Faculty of Medicine
Lund University
Sweden

Professor Raimo Sepponen
Department of Electronics
School of Electrical Engineering
Aalto University
Finland

**Opponent:**

Professor Miika Nieminen
Department of Radiology
Institute of Diagnostics
University of Oulu
Finland

Report Series in Physics HU-P-D220
ISSN 0356-0961
ISBN 978-951-51-0230-0
ISBN 978-951-51-0231-7 (pdf-version)
http://www.ethesis.helsinki.fi
Helsinki University Print
Helsinki 2014

**S. Strengell**: Characterization of synchrotron radiation based functional lung imaging, University of Helsinki, 2014, 50 pages. University of Helsinki, Report Series in Physics, HU-P-D220

**Keywords:** Synchrotron radiation, CT, dosimetry, xenon, K-edge subtraction, distribution of ventilation, asthma

**Classification (INSPEC): A8700, A8760M, B7530, B7510P**

# Abstract

Functional lung CT using synchrotron radiation was applied for studying regional ventilation distribution *in vivo* in animal lungs. This quantitative method employs the K-edge subtraction (KES) technique, which takes advantage of the sharp rise of the absorption coefficient at the binding energy of K-shell electron of a contrast agent. In KES technique two images are taken simultaneously at energies bracketing the K-edge energy of stable xenon (Xe) gas. This technique produces absorption CT images for structural evaluation and Xe density images and at the same time it allows the study of the regional ventilation heterogeneity, calculated based on wash-in series of Xe inhalation images.

In this work the analysis of KES CT images was developed to show the regional differences in the airway reactions produced by the direct constrictor agonist, methacholine (MCh), and the indirect constrictor agonist, ovalbumin (OVA), in healthy and ovalbumin sensitized rabbits. Moreover these constrictors were tested under the influence of cigarette smoke. The effect in airways of different administration routes of MCh, inhaled or intravenous (i.v.), was studied using low radiation dose Xe density CT images. The radiation dose in synchrotron radiation imaging of rabbit lungs *in vivo*, with and without Xe, was calculated and measured using several methods and compared to the image quality.

Results showed that i.v. MCh caused bronchoconstriction primarily in central airways in healthy and asthmatic animals, whereas i.v. OVA only in asthmatic animals. Inhaled MCh, in both groups, affected more the periphery. On the other hand cigarette smoke inhibited the bronchoconstriction in both healthy and ovalbumin sensitized animals. Theoretical and measured values of synchrotron radiation dose were consistent in this setup. Dose dependency of the image quality, defined by signal to noise ratio, was evaluated, and a threshold for detectable signal contrast was found. The optimal imaging setup was estimated using these results.

These findings show the feasibility of the KES CT method for functional lung imaging of airway reactions by providing information on the regional ventilation distributions. By optimizing the image acquisition and reconstruction algorithms with existing methods, KES CT lung imaging could be adaptable for human studies in the near future.

# Preface

This thesis is based on a research collaboration between the Department of Physics at the University of Helsinki (HU, Finland) and the Medical Beamline ID17 at the European Synchrotron Radiation Facility (ESRF, Grenoble, France). I thank the previous and current heads of the Department Prof. Juhani Keinonen and Prof. Hannu Koskinen for providing the opportunity to work at the Department of Physics, and Prof. Ritva Serimaa for all her support at the Division of Material Physics. I gratefully acknowledge the Ida Montin Foundation, Tampere Tuberculosis Foundation, University of Helsinki and the Academy of Finland.

I express my gratitude to the official reviewers of the thesis: Prof. Per Wollmer and Prof. Raimo Sepponen for their valuable comments and constructive criticism.

Special thanks go to my supervisors Prof. Anssi Sovijärvi and Dos. Liisa Porra, as well as Prof. Pekka Suortti, for introducing me to a fascinating world of medical physics. I am deeply grateful for your guidance and encouragement throughout this work. I would also like to express thanks to Prof. Sam Bayat for all the help and laughs that you gave me during our experiments. Without you all this work could not be feasible.

I wish to thank my teammates in Helsinki, Heikki and Jani, for the fruitful conversations and valuable co-operation. I wish to also thank the FOT team and personnel of the ESRF, especially Christian Nemoz for salmiakki-smelling computational help and Herwig Requard for technical help even at Sunday 2 am. Great thanks go to William Thomlinson, who helped me to make this thesis better.

Many thanks are due to my colleagues at Helsinki University Central Hospital. It has been a pleasure to share the inspiring atmosphere and enjoyable moments with you during all these years. I truly enjoy working with you.

Ever since I first joined the material physics lab at HU as an outsider from Turku I always had lunch company. Thank you for the relaxed and vivid conversations.

I owe a great deal to my friends in Joensuu, Turku and Helsinki. Thank you for sharing some of the most precious moments of my life. I would like to thank my parents Aini and Pekka and my sisters Mari and Tiina for their absolute and selfless support during these years. Without you I wouldn't even have gotten to do this.

Finally and most importantly, I owe my deepest gratitude to my husband Juha. His unlimited patience, kind understanding and endless love have been my strongest support. Together we have been privileged to raise daughters, Mila and Elena. Their unconditional love and inspiring way to see life have been the greatest joy in my life.

Helsinki, September 2014

# List of original articles

This thesis consists of an introduction and four articles, which are referred to by the roman number numerals **I – IV** throughout the text.

**I** Bayat, S., **Strengell, S.**, Porra, L., Janosi, T., Petak, F., Suhonen, H., Suortti, P., Hantos, Z., Sovijärvi, A. & Habre, W. (2009). Methacholine and ovalbumin challenges assessed by forced oscillations and synchrotron lung imaging. *American Journal of Respiratory and Critical Care Medicine*, 180(4):296-303.

**II** Porra, L., Petak, F., **Strengell, S.**, Neitola, K., Janosi, T. Z., Suhonen, H., Suortti P., Sovijarvi, A. R. A., Habre, W. & Bayat, S. (2010). Acute cigarette smoke inhalation blunts lung responsiveness to methacholine and allergen in rabbit : differentiation of central and peripheral effects. *American Journal of Physiology: Lung Cellular and Molecular Physiology,* 299(2):242-251.

**III** **Strengell, S.**, Porra, L., Sovijärvi, A., Suhonen, H., Suortti, P. & Bayat, S. (2013). Differences in the pattern of bronchoconstriction induced by intravenous and inhaled methacholine in rabbit. *Respiratory Physiology & Neurobiology*,189(3):465-472.

**IV** **Strengell, S.**, Keyriläinen, J., Suortti, P., Bayat, S., Sovijärvi, ARA., Porra, L. (2014). Radiation dose and image quality in K-edge subtraction CT of lungs *in vivo*. *Journal of Synchrotron Radiation, in press,* 21(6).

# Symbols and abbreviations

| | |
|---|---|
| $C_{K,PMMA,w}$ | Computed tomography index, weighted (CTDI, $C_D$) |
| CA | Cross sectional area |
| COPD | Chronic obstructive pulmonary disease |
| CS | Cigarette smoke |
| CT | Computed tomography |
| CV | Coefficient variation |
| D | Absorbed dose |
| DECT | Dual energy computed tomography |
| ESRF | European synchrotron radiation facility |
| FBP | Filtered back projection |
| FOT | Forced oscillation technique |
| Ge | Germanium |
| HRCT | High resolution computed tomography |
| HU | Hounsfield unit |
| i.v. | Intravenous |
| $K_a$ | Air kerma |
| KES | K-edge subtraction |
| MCh | Methacholine |
| MDCT | Multi-detector computed tomography |
| MECT | Multi-energy computed tomography |
| Micro-CT | Micro computer tomography |
| MRI | Magnetic resonance imaging |
| MTF | Modulation transfer function |
| OVA | Ovalbumin |
| $P_{KL}$ | Air kerma length product |
| PET | Positron emission tomography |
| PMMA | Polymethyl methacrylate |
| SNR | Signal to noise ratio |
| SPECT | Single photon emission computed tomography |
| $s\dot{V}$ | Specific ventilation |
| VA | Ventilated alveolar area |
| VD | Ventilation defect |
| Xe | Xenon |

# Contents

# 1 Introduction

The prevalence of asthma in children and adults is 4.3 % worldwide [WHO, 2007] and 9.4 % in Finland [Pallasaho et al., 2011]. Respiratory diseases, including asthma, are the third in mortality rates in Europe [Eurostat, 2014]. Asthma is amongst the most common chronic disorders affecting humans and accounts for considerable morbidity and mortality worldwide, but the mechanisms of this lung disease are not fully elucidated. Asthma induces non-uniform bronchoconstriction and thus disturbance to the regional distribution of ventilation. While the structure of the lungs in acute asthma reactions does not change, the ventilation becomes heterogeneous. This emphasizes the need for an adequate imaging method to study both structure and function of the lung at the same time.

Functional lung imaging has been challenging with clinically available methods, such as magnetic resonance imaging and nuclear medicine imaging because of the weak signal from the contrast gas, texture of the lung tissue and alveolar airspaces, or the movements of the lungs and the heart. Changes in lung structure are usually studied by x-ray computed tomography (CT) imaging. CT imaging has good spatial and time resolution, but disadvantages are the radiation dose and weak signal of the lungs without an appropriate contrast agent.

K-edge subtraction (KES) CT imaging with xenon (Xe) as a contrast agent is a novel and unique technique that uses monochromatic synchrotron radiation imaging. KES CT is a non-invasive imaging method for simultaneous imaging of lung structure and function [Bayat et al., 2001]. The great advantage of KES CT as a functional lung imaging method is that it allows direct quantification of the Xe density in air spaces of alveoli and airways. A disadvantage of this method is the radiation dose from the synchrotron radiation beams.

At the moment KES CT lung imaging has been used only for scientific purposes in animal studies without too much attention to the radiation dose, but the possibility of using KES CT in human studies raises the question of the radiation dose caused by the imaging. This is particularly important, as with the advent of compact synchrotron radiation sources, a wider availability of this imaging modality can be expected in the future [Achterhold et al., 2013].

# 2 Background

## *2.1 Methods for functional lung imaging*

Physiology of the lungs, diagnosis and characterization of lung diseases are studied using pulmonary imaging methods and non-imaging methods such as spirometry, the forced oscillation technique, and multiple breath wash-out studies. Non-invasive conventional methods, like spirometry, measure lung function at the mouth level, and information comes from the whole lung at the same time, even though in healthy lungs, not to mention in diseased lungs, the function of the lung is in fact regionally heterogeneous [Tzeng et al., 2009]. Also a forced expiratory maneuver, used in standard airflow measurement, may skew the results of lung function measurement by relying on a single summation measure of airflow [Thien, 2013] and by inducing airway compression thus decreasing the airflow [Piirilä et al., 2014]. Methods to study ventilation heterogeneity of the lung, such as measurements of lung mechanics and multiple breath inert gas wash-out provide only global and indirect evaluation of the heterogeneity of lung function. Structural changes assessed by image-based methods, such as computed tomography, nuclear medicine imaging and MRI, have the potential to provide limited quantitative information on the spatial characteristics and heterogeneity of ventilation.

### *2.1.1 Imaging with radioactive tracers*

Nuclear medicine imaging is used to measure the distribution and intensity of radionuclides inside the lungs. For ventilation studies radionuclear scintigraphy using gamma cameras is used for taking static planar lung images over time for indicating wash-in and wash-out of the inhaled radioaerosol or gas.

In radiospirometry the ventilation can be studied by radioactive gases, $^{133}$Xe, $^{81}$Kr, or $^{99}$Te aerosol, with extra-thoracic gamma detectors and distributions of ventilation, lung volumes and perfusion can be measured [Sovijärvi et al., 1982, 1986].

SPECT (Single Photon Emission Computed Tomography) generates 3D images of the distribution of inhaled radioisotopes in the body by a rotating gamma camera and acquiring projection images. In functional lung imaging commonly used radioactive tracers are $^{133}$Xe, $^{127}$Xe and $^{81m}$Kr gases and dispersed $^{99}$Tc [Zhang et al., 2008]. The radiation dose delivered by imaging is about 1-5 mSv, which corresponds to the doses from thorax CT.

Another functional nuclear medicine imaging modality, PET (Positron Emission Tomography) uses short lived positron emitters such as $^{18}$F, $^{13}$N,$^{15}$O, $^{68}$Ga and $^{19}$Ne as a tracer. It is based on the detection of radiation from the annihilation of these positrons, when they interact with an electron in the tissue. The annihilation process yields two 511 keV photons that are ejected in opposite directions and detected by high-energy gamma detectors. Ventilation and also perfusion can be measured with intravenous (i.v.)

infusion of $^{13}N_2$ during a breath hold after receiving the tracer. Alveolar concentration of the tracer rises until the plateau is reached. The wash-out phase starts when the patient resumes breathing and tracer concentration decreases as the tracer is removed by ventilation. Ventilation can be assessed using the wash-out data [Zhang et al., 2008].

The downside of these modalities is the use of ionizing radiation due to the radioactive contrast agents. Besides having limited spatial and temporal resolution, quantitation of these modalities is related to scatter and attenuation corrections [Petersson et al., 2007]. In experimental setups for animals, using SPECT, 0.35 mm resolution can be reached for 5 seconds per rotation, but with very low statistics [Rahmim and Zaidi, 2007]. In clinical settings the resolution is 1 cm and the imaging time is about 10 minutes. When using PET, even in theory, it is not possible to reach higher resolution than 1.5 mm because of the positron path length in lung tissue [Sánchez-Crespo et al., 2004]. In clinical PET solutions the resolution rises to 5 mm [Tai and Laforest, 2005].

### *2.1.2 Magnetic resonance imaging (MRI)*

The advantage of magnetic resonance imaging (MRI) is that this imaging modality does not use ionizing radiation. MRI employs the energy of oscillating magnetic fields to visualize the body by detecting the radio frequency signal emitted by hydrogen atoms, which are present in water containing tissue. Lungs are a challenging target to image using MRI, since the hydrogen level is low in the lung tissue. The chest and heart motions, and air filling in the airways, cause artefacts.

Appropriate image quality in lung imaging with MRI requires a contrast agent and for that a hyperpolarized noble gas is used as signal emitting target [Fain et al., 2007, Tzeng et al., 2008]. Most commonly used hyperpolarized noble gases are $^{3}He$ [Middleton et al., 1995], $^{129}Xe$ [Albert et al., 1994] and $^{19}F$ using sulfur hexafluoride ($SF_6$) [Kuethe et al., 2000]. Also, the paramagnetic properties of $O_2$ have been used to visualize the airways [Edelman et al., 1996, Ohno et al., 2011].

The achieved spatial resolution of hyperpolarized gases in 3D MRI is at best (0.125 x 0.125 x 1) $mm^3$ in mice in a 5.8 min acquisition using hyperpolarized $^{3}He$ [Driehuys et al., 2007]. Higher temporal resolution can be reached when imaging a small volume or single slice [Levin et al., 2001]. Besides consuming large quantities of hyperpolarized $^{3}He$, the imaging of large volumes also takes considerable time, because these methods require multiple images to be acquired for averaging a single breath [Mistry et al., 2010]. Another disadvantage is that images produced by MRI are not quantitative and the exact amount of the contrast agent is not possible to measure and therefore measurements are non-reproducible [van Beek and Hoffman, 2008].

### *2.1.3 Computed tomography (CT)*

Computed tomography techniques using x-rays, conventional CT, multi-detector CT (MDCT), high-resolution computed tomography (HRCT), micro computed tomography

(micro-CT) and dual energy computed tomography (DECT) images are quantitative and have superior space and temporal resolution. CT methods are widely used in hospitals for structural lung imaging but they also can be used for functional lung imaging with or without a contrast agent [Guerrero et al., 2006].

A commonly used contrast agent is stable, non-radioactive, Xe gas, which is highly absorbing for x-rays at and above the K absorption energy. Xe enhanced CT [Gur et al., 1979] is possible to do using any of the CT modalities, but as of now there are no lung studies made with micro-CT using Xe as contrast agent. While non-contrast CT images are quantitative, Xe enhanced CT does not produce quantitative Xe images, but only relative densities of Xe which can be used for estimating the Xe concentration during ventilation [van Beek and Hoffman, 2008]. The density of Xe increases linearly in conjunction with Xe concentration in the lungs when measured in Hounsfield units (HU) [Marcucci et al., 2001]. Regional ventilation is measured from the time course of cine-CT density change during a multibreath wash-in and wash-out of Xe [Ley-Zaporozhan et al., 2008]. CT modalities also use subtraction imaging where the subtraction is made of the images taken before and after inhaling Xe gas. There are crucial movement artefacts involved in this method, because images are not taken simultaneously. The contrast enhancement during 30 % Xe inhalation with a standard CT machine is less that 50 HU [Chon et al., 2007].

More recent quantitative CT imaging techniques are dual and multi energy computed tomography (DECT, MECT). The DECT technique uses two, and MECT several different x-ray energy spectra, which allows the separation of different tissues with the same density. Dual and multi energy techniques are based on the fact that attenuation of x-ray photons is energy-dependent and each substance has a specific attenuation curve [Avrin et al., 1978]. To avoid the temporal changes of images with different energy spectra, images are taken simultaneously using dual-source CT. In addition to the information obtained by DECT, MECT allows the spectral decomposition of more than one element with a high atomic number [Roessl et al., 2007]. DECT is also used with Xe as a contrast agent [Chae et al., 2008]. The contrast element can be subtracted by reconstructing a virtual non-contrast-enhanced image. A disadvantage of this technique is that materials with similar attenuation curves cannot be distinguished [Fornano et al., 2011]. The energy spectrum of x-rays from conventional sources is wide and non-monochromatic, which causes artefacts in the images and increases the error of concentration measurements.

The achieved spatial resolution for structural images in micro-CT is (28x28x28) $\mu m^3$ [Thiesse et al., 2010] and for perfusion images, using liposomal contrast agent, the spatial resolution is 176 μm and the temporal resolution is 687 ms. A single rotation requires 22 seconds and permits 440 projections using dual source micro-CT [Badea et al., 2011]. The spatial resolution in ventilation images with Xe as a contrast agent is 153x153x153 $\mu m^3$ [Santyr et al., 2011]. A typical radiation dose for micro-CT perfusion images is 0.06 Gy per rotation [Badea et al., 2011], and in ventilation images the entrance dose is 0.055 Gy [Santyr et al., 2011]. Typical radiation doses for thorax CT

are 2-6 mSv [Huda, 2007], which corresponds to 2-6 mGy when imaging with conventional x-rays.

### *2.1.4 Combination of imaging modalities*

Since each imaging modality has limitations, a combination of modalities is commonly used. Being an imaging modality, which gives information on the functional parameters but is lacking structural information, CT is a typical combination modality. As well as PET and SPECT, MRI imaging also benefits from the fusion with CT. Registration of the image data and combination of structural and functional images partially compensates for the inadequacies of a single modality but there are problems with the combination of modalities. Even if the images of different modalities are taken using the same scanner, they are not taken at the same time, and this creates movement artefacts between the images. Also differences in the calibration between two modalities may cause an error in the registration of the images.

## *2.2 History of K-edge subtraction imaging*

Originally the idea of K-edge imaging was created in the early 1950's by Jacobson [Jacobson, 1953], who introduced a dual energy K-edge subtraction method for detecting iodine using characteristic x-ray beams emitted from iodine and cerium. In the 1970's anatomical *in vivo* KES images were taken of monkeys using iodine as a contrast agent with two temporally separated beams of different energy [Kruger et al., 1977]. Not until the 1980's, when synchrotron radiation beams became available, could the KES method be performed with two truly simultaneous monochromatic beams [Thompson et al., 1984]. The method was applied in human coronary angiography at Stanford Synchrotron Radiation Laboratory (SSRL), at the National Synchrotron Light Source (NSLS) and at Hasylab [Rubenstein et al., 1986; Suortti et al., 1993; Thomlinson et al., 1996; Dix et al., 1995]. Also, human lung imaging with Xe has already been demonstrated by Giacomini et al. [1998]. At the European Synchrotron Radiation Facility (ESRF) the KES imaging method, using synchrotron radiation, was originally developed for human i.v. coronary angiography with iodine [Elleaume et al., 2000a] or gadolinium [Le Duc et al., 2000] as the contrast agent. The setup was modified for rabbit lung imaging with Xe by our group [Bayat et al., 2001].

The feasibility of KES CT using synchrotron radiation for measuring the quantitative function and structure of airways with excellent spatial resolution has been shown previously [Porra et al., 2004]. Distribution of ventilation has been imaged in healthy rabbits [Porra et al., 2004]. Bronchoconstriction caused by inhaled histamine has been studied by measuring regional lung volume [Monfraix et al., 2005] and kinetics of the changes in airway sizes [Bayat et al., 2006].

## *2.3 Experimental studies of airway reactions*

Bronchial obstruction and lung dysfunction are hallmarks of obstructive pulmonary

diseases such as asthma, bronchiectasis and chronic obstructive pulmonary disease (COPD). Airway reactions, i.e. bronchoconstriction, can also be detected during environmental exposures, i.e. cigarette smoke. While the reactions are studied by challenging the airways with agonists, the cigarette smoke has been determined to induce sensitivity to airway reactions [Juusela et al., 2013]. In addition to lung imaging, airway reactions of the lungs may be studied *in vivo* by investigating histological and biochemical changes in the airways and regional ventilation distribution.

### *2.3.1 Human studies*

Airway reactions have been studied in humans using the previously mentioned imaging methods: hyperpolarized $^{3}$He [Costella et al., 2012] and oxygen-enhanced MRI [Ohno et al., 2011], HRCT [King et al., 2004], DECT [Chae et al., 2010], nuclear medicine scintigraphy [Pellegrino et al., 2001] and PET [Venegas et al., 2005]. Non-imaging methods are also used, e.g. single and multiple breath nitrogen wash-out [Farah et al., 2011], spirometry and the forced oscillation technique (FOT) [Peták et al., 2012]. In the human studies the subjects had already been diagnosed with having an obstructive disease so that the experiments were designed in such a way that no permanent harm could occur. However, the imaging modalities applied for human studies are not able to reach high enough spatial resolution for direct quantitative functional images. Therefore the role of the small airways, smaller than 2 mm, in the disease process of respiratory dysfunction has not been fully resolved.

### *2.3.2 Animal studies*

No single animal model is able to reproduce all the features of human lung function. In animal studies the choice of the animal model is critical. Mice, rats, guinea pigs, rabbits, pigs and even dogs and sheep have been used in pulmonary studies with various conclusions. Due to similarities with the responses observed in human patients the rabbit model has been extensively used in lung studies in assessing the effects of various classes of drugs, airway inflammation and airway responses to various stimuli [Keir and Page, 2008].

### *2.3.3 Smooth muscle constriction agonists*

In the case of acute reaction airway narrowing, airflow limitation and increased airway resistance in bronchoconstriction are studied by contracting the airway smooth muscle. Challenging the airways with a variety of constrictor agonists and natural stimuli can constrict smooth muscle. As direct constrictors, methacholine (MCh) and histamine are commonly used in experimental bronchoconstriction studies. MCh constricts smooth muscle by stimulating muscarinic cholinergic receptors [Roffel et al., 1990]. As an indirect stimulus, ovalbumin (OVA) is used to show the airway reactions to an allergen in animal models, when the subject is sensitized to OVA.

### *2.3.4 Administration routes of airway active molecules*

Besides the choice of the constrictor drug and animal model, the administration route of the drug affects the results. We have used two administration routes: i.v. and inhaled. Inhaled MCh is standardized and commonly used to assess bronchial hyper-responsiveness in diagnosing asthma in humans [Juniper et al., 1981; Crapo et al., 2000]. I.v. MCh has been used in experimental studies in various species, where bronchial response to direct stimuli on smooth muscle in the airways has been evaluated [Martin et al., 1988; Habre et al., 2010]. MCh has been reported to induce an increase in pulmonary resistance in both administration routes in mice [Ameredes, 2004]. Pulmonary resistance increased after MCh was administered as inhaled aerosol or i.v. There was also an increase in parenchymal elastance after inhaled but not after i.v. MCh as assessed by the forced oscillation method in rats [Peták et al., 1997]. When measuring tracheal and alveolar pressure, aerosolized MCh has been demonstrated to have a greater effect on airways than i.v. administration, whereas i.v. MCh had a higher effect in the parenchyma of rats [Nagase et al., 1994]. On the other hand, in humans after inhaled MCh no response was obtained in the parenchymal hysteresis, but airway constriction was observed [Pellegrino et al., 1994].

### *2.3.5 Studies in vitro*

*In vitro* studies of airway reactions, where the lung is isolated from the central nervous system and blood circulation, show that the lung structure can change [Wohlsen et al., 2003], and therefore these methods are not as reliable as *in vivo* methods.

# 3 Aims of the study

These studies were designed to:

- Develop analyzing methods for KES imaging to assess the quantitative distribution of lung ventilation and regional volumes.
- Study airway function and ventilation heterogeneity in healthy and ovalbumin sensitized (asthmatic) animals during methacholine, ovalbumin and cigarette smoke challenge.
- Develop a protocol to measure the radiation dose of KES imaging of lungs.
- Study the relationship between acquired image quality and the radiation dose.

# 4 Materials and methods

## *4.1 KES-imaging method using xenon (Xe)*

The K-edge subtraction CT imaging is a synchrotron radiation imaging technique, where inhaled Xe gas is used as the contrast agent. In the KES method dual monochromatic x-ray beams at two slightly different energies, below and above the Xe K-edge, are used for imaging. Subtraction of these two simultaneously taken images allows the direct quantitative density measurement and visualization of Xe gas.

The quantitative measurements of Xe distribution can be derived from attenuation of monochromatic beams in a subject. Attenuation of the beam in a subject is defined as the change of intensity $I$ of the transmitted x-ray beam [Cullity, 1978]

$$I = I_0 e^{-\mu x}, \tag{4.1}$$

where $I_0$ is the intensity of the incident x-ray beam, $\mu$ is the absorption coefficient and $x$ is the path length through the subject. Typically the imaged object consists of more than one material, therefore equation (4.1) can be extended to include all constituent materials. The intensity change can be calculated for each material (j) with specific density $\rho$, and attenuation coefficient $\mu/\rho$. The total transmitted intensity is a sum of these

$$I_{tot} = I_0 \exp\left[-\sum_j \left(\frac{\mu}{\rho}\right)_j \rho_j x_j\right] \tag{4.2}$$

The measurement of the Xe distribution takes advantage of the sharp rise of attenuation coefficient of Xe at the energy of the K-absorption edge. Photons with energy above the binding energy of the K-shell electrons, are absorbed by the Xe atom due to the photoelectric effect. This causes a sudden rise of the photon attenuation when the energy of the incident x-ray beam crosses at the Xe K-edge energy threshold of 34.56 keV [NIST, 2014]. In a typical setup the energy band width of one beam is 170 eV, and the energy difference of two monochromatic X-ray beams is 250 eV. Around these energies the attenuation coefficient in soft tissue changes from 0.332 $cm^2g^{-1}$ to 0.326 $cm^2g^{-1}$ and in bone from 1.044 $cm^2g^{-1}$ to 1.011 $cm^2g^{-1}$, but there is a very large increase in the coefficient of Xe from 6.13 $cm^2g^{-1}$ to 33.16 $cm^2g^{-1}$. The change of attenuation coefficient in soft tissue is 0.9 %, in bone 1.8 % and in Xe 540%. Therefore in the subtraction image the effect of the residual tissue, i.e. soft tissue and bone, can be neglected and the change of the intensity can be approximated using only the Xe attenuation coefficient

$$\Delta\left[\ln\left(\frac{I}{I_0}\right)\right] = \left(\frac{\mu}{\rho}\right)_{Xe} \Delta(\rho_{Xe} x_{Xe}) \tag{4.3}$$

The mass attenuation coefficient curves of Xe, bone and soft tissue are shown in Figure 4.1.

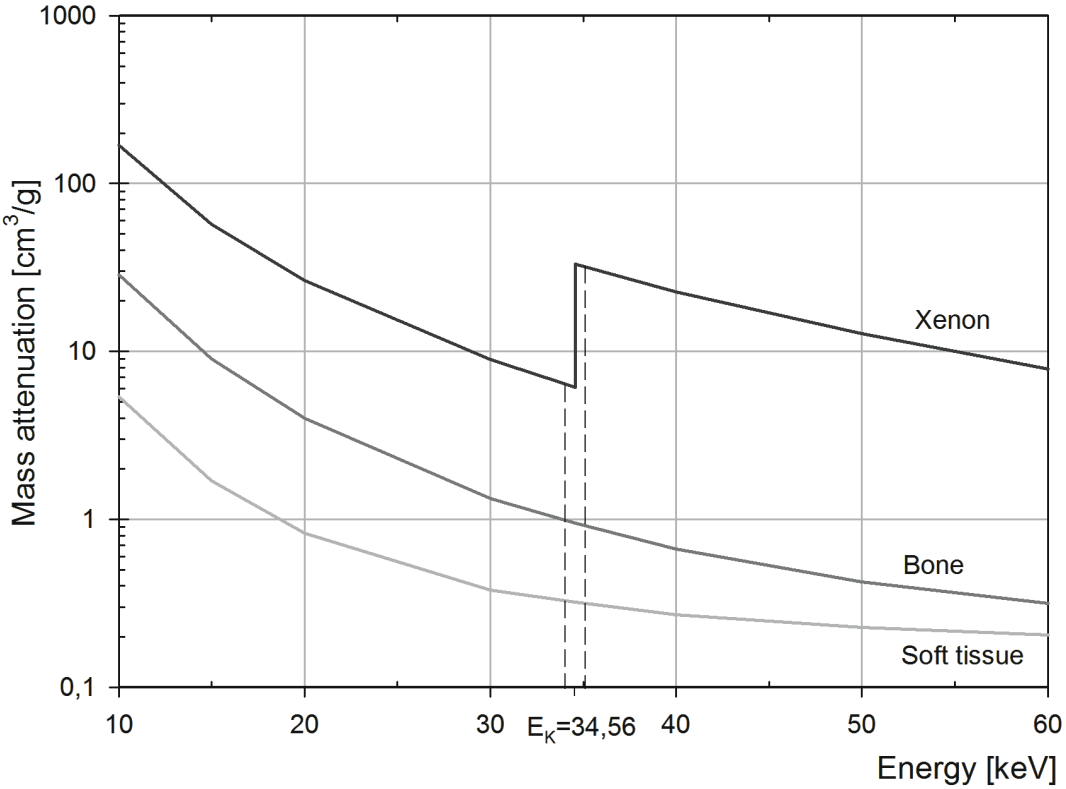


**Figure. 4.1.** Mass attenuation coefficient of xenon, bone and soft tissue. Energy of xenon K-edge is $E_K$ = 34.56 keV. Dashed lines indicate the energies of the two imaging bands.

The density of Xe, $\rho_{Xe}$, can be calculated directly from the subtracted CT images, since the path length, that is pixel size, is known.

## *4.2 Beamline instrumentation*

All experiments in this series of study were performed at the Bio-medical Beamline (ID17) of the European Synchrotron Radiation Facility (ESRF), Grenoble, France, which is dedicated to clinical and preclinical medical applications of synchrotron radiation. A detailed description of the instrumentation of the beamline is reported in Elleaume et al. [1999].

### *4.2.1 Synchrotron radiation beam*

KES CT imaging takes advantage of the intensity of synchrotron radiation beam allowing the selection of monochromatic radiation from the white beam [Suortti and Thomlinson, 2003]. The flux of the continuous spectrum of synchrotron radiation beam is 100000 times higher than the beam produced by typical x-ray tubes in hospital scanners. At the ESRF synchrotron electrons are produced by an electron gun and directed to a linear accelerator where a thin beam of electrons packed in bunches is accelerated inside a vacuum tube with pulsed microwaves to near the speed of light. These electron bunches are guided to a booster ring where they are accelerated to 99.9997 % of the speed of light by radio frequency cavities. After reaching 6 GeV in 50 ms, electron bunches are injected into the storage ring where the electrons pass through bending and focusing magnets, wiggler magnets, and undulator magnets. By bending of the path of the electron bunches multiple times, a wiggler with 21 poles and a maximum 1.4 T magnetic field produces the radiation beam in the forward direction. The x-ray beam is directed in the vacuum tube to the experimental imaging hutch, which is situated at 150 meters from the source of the beam. At that location the beam is horizontally 150 mm (1 mrad) wide and vertically nearly parallel. The layout of the synchrotron radiation facility is shown in Figure 4.2.

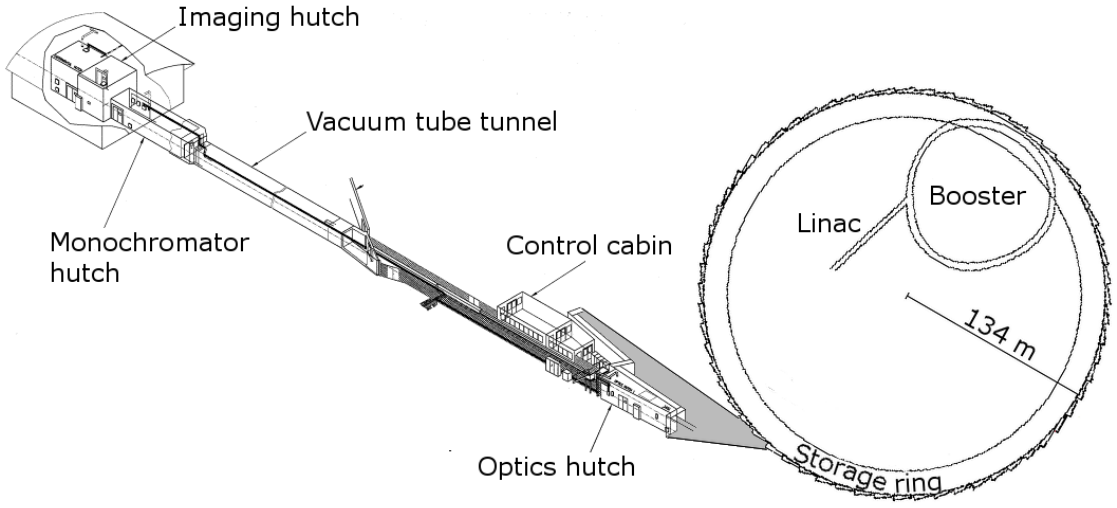


**Figure 4.2.** Overview of the European Synchrotron Radiation Facility (ESRF) and the medical beamline ID17.

The characteristic energy of the continuous spectrum of the ID17 beam is 17.36 keV at a wiggler gap of 55 mm. When exiting the storage ring, the beam passes through an optics hutch, where the beam's vertical and horizontal dimensions are defined by

primary slits, and where lower energies of the x-ray spectrum are removed by graphite and aluminum filters for protecting the monochromator. The monochromator is a bent Si crystal that selects the narrow band of energies to be used in the experiment.

*4.2.2 Monochromator hutch*

Figure 4.3 shows the instrumentation in the satellite building, which is situated at the end of the vacuum tube in the tunnel.

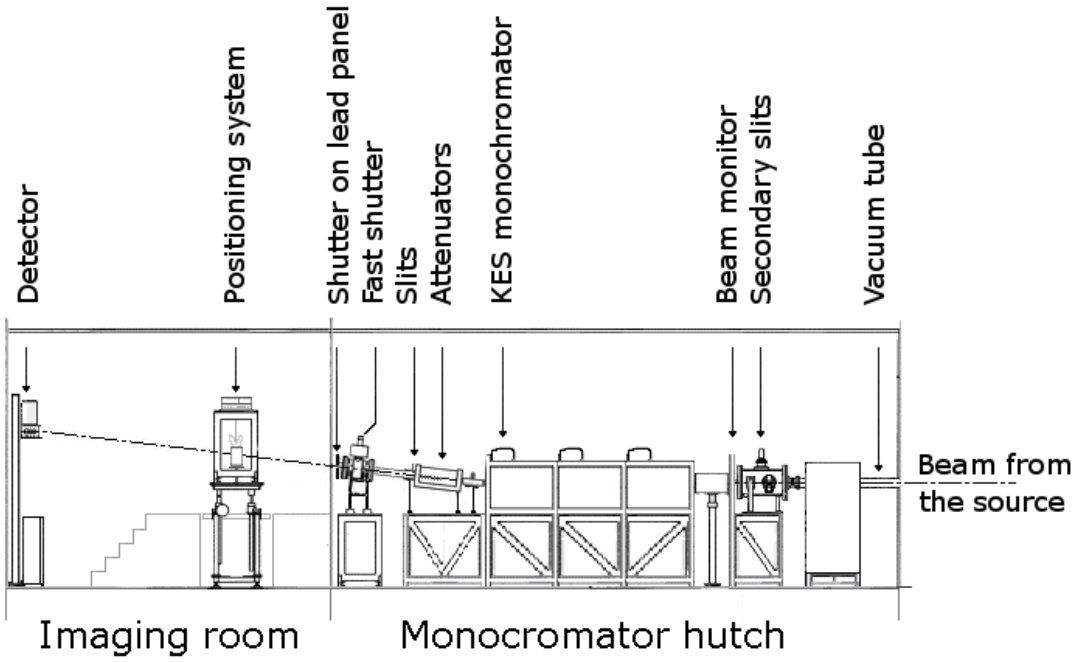


**Figure 4.3.** Instrumentation layout of the monochromator hutch and imaging room in the satellite building.

The radiation fan is limited at the beamline entrance to 1 mrad (horizontal) and 0.067 mrad (vertical). The continuous synchrotron radiation spectrum travels through the vacuum tube to secondary slits and a beam position monitor. The height of the beam is limited to 6.00 mm and then the beam travels to a cylindrically bent silicon crystal transmission monochromator [Suortti et al., 2000]. A Laue-type K-edge monochromator, used in these studies, can be adjusted to select a beam with monochromatic energy from 17 to 51 keV. At the energy of the Xe K-edge, the beam is reflected upwards by 6.56°. After the monochromator, two mono-energetic beams are produced by dividing the beam with a tantalum splitter, which defines the energy separation of the beams. The splitter blocks 2.7 mm at the center of the beam. The width of the energy bands in this configuration is 170 eV and the beams are separated by 250 eV (Figure 4.4).

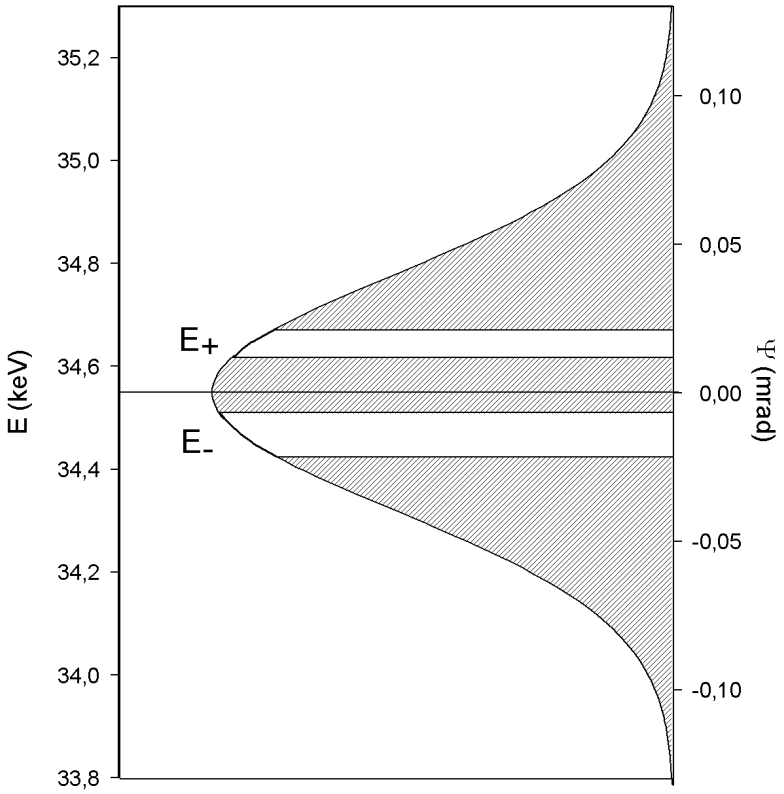


**Figure 4.4.** The vertical profile of the dual beam passed by the slit, monochromator and splitter.

The two separated x-ray beams are attenuated by a Plexiglass attenuator, whose thickness can be varied from 0 cm to 32 cm by steps of 2 cm resulting in a photon flux reduction up to 4 orders of magnitude. Two simultaneously actuating safety tungsten shutters block the beam in case of emergency and a fast imaging shutter, also made of tungsten, limits the x-ray exposure of the imaging object. From the monochromator hutch the beam travels to the imaging hutch, where the experiments are performed.

### *4.2.3 Positioning system for the imaged object*

For recording a two-dimensional image from the static beam it is necessary to move and rotate the imaged object through the beam. The positioning system of experimental setup (Figure 4.5) is a high precision stage, which allows positioning of the object and the scan motions during image acquisition. The system allows rotation around an axis perpendicular to the plane of the beam, two translation movements (X, Y), vertical movement (Z) which is the scan translation direction and rotations around the X and Y axes for alignment with high rigidity. Besides typical 2D slice imaging and vertical scanning of the object, it is possible to acquire 3D helical computed tomography images with this positioning system.

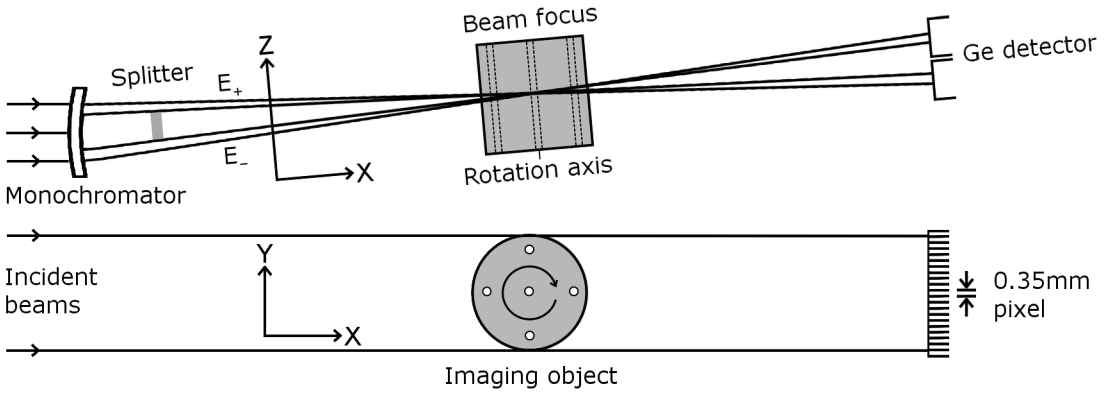


**Figure 4.5.** The experimental setup for imaging and dosimetry. The coordinates are X along the beam direction, Y in the horizontal plane perpendicular to the beam, and Z in the vertical direction. The angular movements around the X and Y axis are used to set the rotation axis perpendicular to the plane of the beam. The imaged object is positioned at the beam focus and rotated around the rotation axis. The PMMA head phantom used in dose measurements has one central and four peripheral holes for the pencil shaped dosimeter. In deep dose measurements the head phantom is replaced by a plane parallel ionization chamber, which is placed behind a stack of PMMA plates.

### *4.2.4 Properties of the detector*

Two monochromatic fan beams produced by the monochromator focus and cross at the center of the positioning system, where the imaged object is located, beyond which they diverge. The beams are detected simultaneously using a liquid nitrogen (-196 °C) cooled high purity germanium (Ge) dual-line detector (EGPS, Eurisys Mesures, Lingolsheim, France). The detector consists of a 160-mm-long monolithic germanium crystal and is electrically segmented into two rows of 432 parallel strips, 0.5 mm apart vertically. The elements are 10 mm high and have a pitch of 0.35 mm. Characteristics for this type of solid-state detector are the direct conversion from photons to electrons, excellent efficiency and wide dynamic range. The efficiency of the detector at 20 keV is nearly 100% and at 99 keV 45% with a Ge crystal thickness of 2.5 mm and beryllium window thickness 0.5 mm. The modulation transfer function of the Ge detector shows the first zero values at 2.9 lp/mm and 5.7 lp/mm, and at 10% level 2.5 lp/mm, 3.2 lp/mm and 5.0 lp/mm [Bravin et al., 2003]. 16-bit dynamic range of the electronics allows recording signals over more than 4 decades. The system has excellent linearity and low noise level, down to about 5 pA [Elleaume et al., 1999]. Horizontal resolution of the detector depends on the spacing of the detector with the image resolution corrected for a small horizontal divergence of the beams. Since this detector integrates all the photon in the vertical direction the vertical resolution is determined by the beam height measured at the object position

### *4.2.5 Properties of the beam*

The beam height at the imaging focus determines the vertical resolution of the images.

The beam height was measured by the germanium detector by scanning a narrow slit situated on the imaging focus across both synchrotron radiation beam in 0.1 mm steps. The height of the beam was defined as an integral width ($\beta_{int}$) [Krill et al., 2000].

$$\beta_{\text{int}} = \frac{\int I_P(x)dx}{\max[I_P(x)]} \tag{4.4}$$

where $I_P(x)$ is the vertical profile of the intensity, where the background noise is subtracted. Total beam height was calculated from average of pixels. For the total beam width the integral height, $\beta_{int}$, is 0.63±0.03 mm (Figure 4.6) and for the center of the beam (± 1 cm) $\beta_{int}$ is 0.625±0.007 mm.

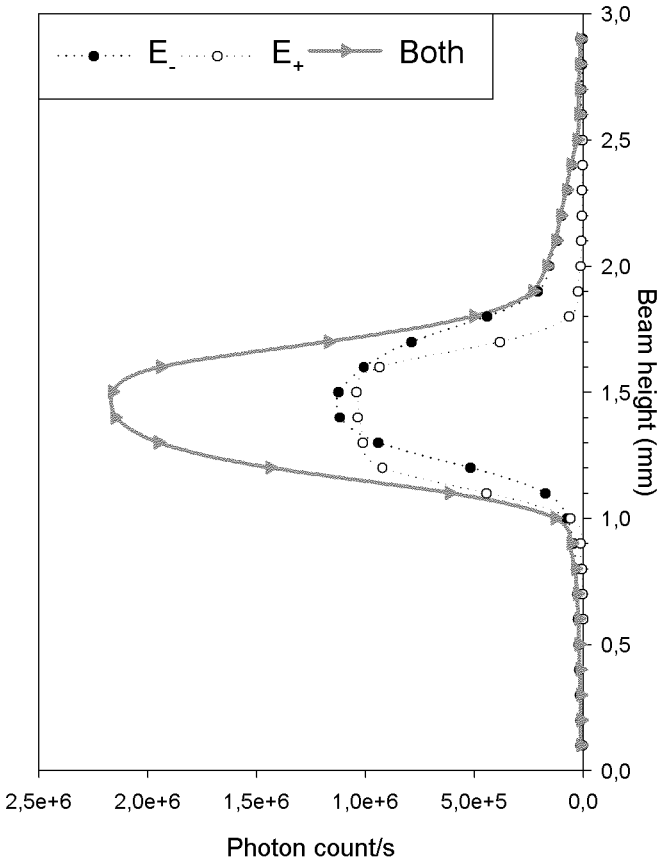


**Figure 4.6.** Vertical scans of the beams at the focus. '-' indicates the beam energy below K-edge of xenon and '+' the beam above K-edge of xenon and "Both" indicates the sum of the beams. Figure adapted from article IV.

The vertically integrated beam intensities are detected by the two pixel rows of the Ge detector (Figure 4.7). The difference in intensity of the beams is due to a small off-centering of the primary slits.

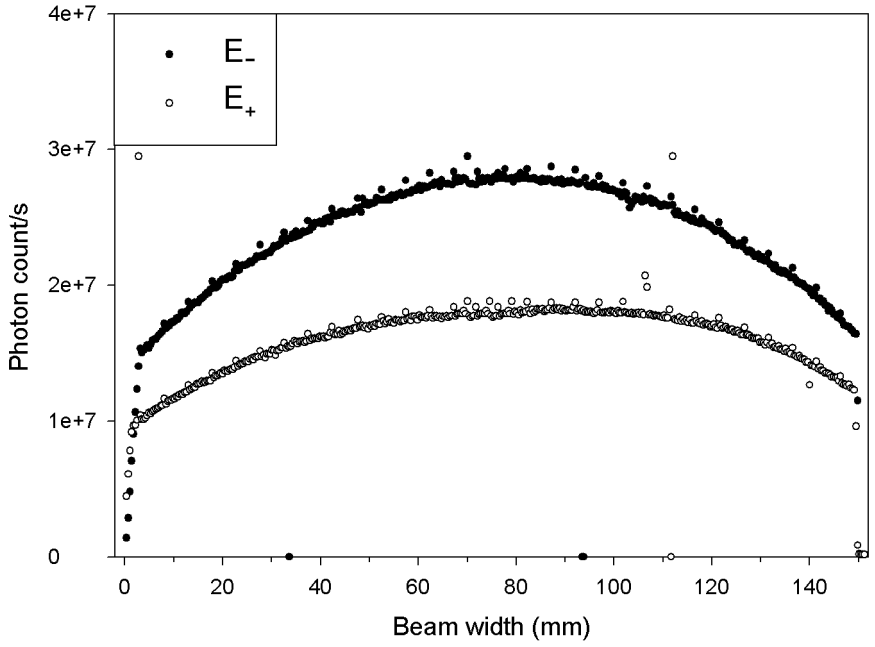


**Figure 4.7**. Horizontal profiles of the beams at the Ge detector. Figure adapted from article IV.

## *4.3 Image processing*

### *4.3.1 Reconstruction of lung tissue and contrast agent images*

In CT imaging the rotation speed was 180° $s^{-1}$ and for a single CT slice 720 projections were recorded at every 0.5°. CT images were reconstructed using a filtered back projection (FBP) [Bracewell and Riddle, 1967], which was applied to the use of KES CT algorithm with the Interactive Data Language (IDL, RSI, Boulogne-Billancourt, France). In FBP the attenuated signal of the projections is transformed to a CT image using the Fourier Slice theorem and high pass filtering before the back projection. The attenuation of the imaging object results in a two-dimensional reconstructed image, and the density, due to contrast agent or tissue, can be calculated from the attenuated signal separately in each voxel using a specifically developed computer algorithm explained in detail by Sarnelli et al. [2005].

The signal detected is proportional to the number of photons, i.e. the intensity *I* after the transmission through the sample. For calculating the photon intensity, equation 4.1. can be written as

$$I_{E_\pm} = I_{0,E_\pm} \exp\left[-\sum_j \left(\left(\frac{\mu}{\rho}\right)_{j,E_\pm} \rho_j x_j\right)\right] + C \qquad (4.5)$$

where $I_0$ is the incident intensity per pixel without the subject, $E_{\pm}$ means the energies above and below the Xe K-edge. $(\mu/\rho)_j$ is the mass attenuations coefficient, $\rho_j$ is the density of the matter, $x_j$ is the transmitted path length, $j$ denotes the different materials or tissues, i.e. contrast agent (Xe or iodine), bone and soft tissue, and $C$ is the dark current of the detector without the beam. Using the dual-energy method [Lehrmann et al., 1981] with two images it is possible to decompose the sample separately into two materials, to contrast agent (Xe or iodine) and to tissue, which consists of the rest of the materials except the contrast agent. With this separation,

$$\ln\left(\frac{I_0}{I}\right)_{E_\pm} = \left[\left(\frac{\mu}{\rho}\right)_{E_\pm} \rho x\right]_{Xe} + \left[\left(\frac{\mu}{\rho}\right)_{E_\pm} \rho x\right]_{Tissue}, \tag{4.6}$$

where $\mu/\rho$ and mass density $\rho x$, are defined at the energies of interest for Xe and for soft tissue, $I_0$ is the white field images acquired without the object. The mass attenuation coefficients of the Xe and tissues are shown previously in Figure 4.1. Mass densities for Xe and tissue in the images are calculated pixel-by-pixel using equation 4.6.

$$(\rho x)_{Xe} = \frac{\left[\left(\frac{\mu}{\rho}\right)_{E_-}\right]_{Tissue} \ln\left(\frac{I_0}{I}\right)_{E_+} - \left[\left(\frac{\mu}{\rho}\right)_{E_+}\right]_{Tissue} \ln\left(\frac{I_0}{I}\right)_{E_-}}{\left[\left(\frac{\mu}{\rho}\right)_{E_-}\right]_{Tissue}\left[\left(\frac{\mu}{\rho}\right)_{E_+}\right]_{Xe} - \left[\left(\frac{\mu}{\rho}\right)_{E_+}\right]_{Tissue}\left[\left(\frac{\mu}{\rho}\right)_{E_-}\right]_{Xe}} \tag{4.7}$$

$$(\rho x)_{Tissue} = \frac{\left[\left(\frac{\mu}{\rho}\right)_{E_+}\right]_{Xe} \ln\left(\frac{I_0}{I}\right)_{E_-} - \left[\left(\frac{\mu}{\rho}\right)_{E_-}\right]_{Xe} \ln\left(\frac{I_0}{I}\right)_{E_+}}{\left[\left(\frac{\mu}{\rho}\right)_{E_-}\right]_{Tissue}\left[\left(\frac{\mu}{\rho}\right)_{E_+}\right]_{Xe} - \left[\left(\frac{\mu}{\rho}\right)_{E_+}\right]_{Tissue}\left[\left(\frac{\mu}{\rho}\right)_{E_-}\right]_{Xe}} \tag{4.8}$$

Since $x$ is the pixel size for CT images, local $\rho_{Xe}$ and $\rho_{Tissue}$ can be solved quantitatively in every pixel of the image.

## *4.4 Image analysis*

Tissue density images are used to study changes in lung structure, and Xe density images are used for functional studies. A Region Growing segmentation algorithm was used to select the lung tissue mask within the tissue density images. In this fashion, major blood vessels and airways were excluded from the analyses and the mask was used in analysis of the corresponding Xe density images.

### *4.4.1 Calculation of specific ventilation images*

The measurement of ventilation distribution is based on a multiple breath model where images are taken during wash-in of the contrast gas (Xe). Imaging starts simultaneously with Xe inhalation, and 8-15 images are recorded until the equilibrium level of Xe density is reached in the lung. Ventilation is paused for three seconds during each image acquisition, and between two images, the animal breaths a few cycles of Xe-O2 mixture. According to a single compartment model, Xe concentration ($c$) in the lungs increases monoexponentially as a function of time ($t$) during the wash-in sequence [Simon et al., 1985, Porra et al., 2004]. This is represented by

$$c(t) = c_A\left[1 - \exp\left(-\frac{t - t_0}{\tau}\right)\right], \tag{4.9}$$

where $c_A$ is the asymptotic concentration, which is reached in the equilibrium level of Xe in the lung, $\tau$ is a local time constant and $t_0$ is an arrival time, which includes the transfer time from the gas valve through the trachea to the entrance of the acini in the region of interest.

Using equation 4.9 the time constant $\tau$ can be calculated by fitting an exponential curve to the measured Xe concentration curve with multidimensional unconstrained non-linear minimization (Nelder-Mead). To minimize the effects of statistical truncations and image registration errors, Xe density images were smoothed with a 5 × 5 pixel moving average prior to the analysis. The local specific ventilation $s\dot{V}$, which is the ventilation normalized to the gas volume within the voxel, is the inverse of the time constant. $s\dot{V}$ can be calculated for each voxel in the lungs separately during the wash-in period and combined to produce specific ventilation images.

### *4.4.2 Estimation of ventilation based on single Xe images*

Multiple breath models require several CT images, which leads easily to high radiation exposures. For reducing radiation dose, image acquisition time and use of Xe gas, regional ventilation can be estimated reasonably well from a single Xe density image that is acquired before the equilibrium of Xe concentration is reached in the lungs. For the best estimate images should be taken at 75% of equilibrium of Xe concentration [Porra et al., 2009]. In this case the slow ventilation zones are shown as low Xe concentration in the images.

### *4.4.3 Analysis of ventilation images*

The statistical distribution of the regional ventilation can be described using a log-normal function due to the fractal structure of the bronchial tree [Majumdar et al., 2005]. This model was used to determine normally ventilated zones. For each ventilation image a histogram of $s\dot{V}$ was calculated and a log-normal function was

fitted to the histogram (Figure 4.8).

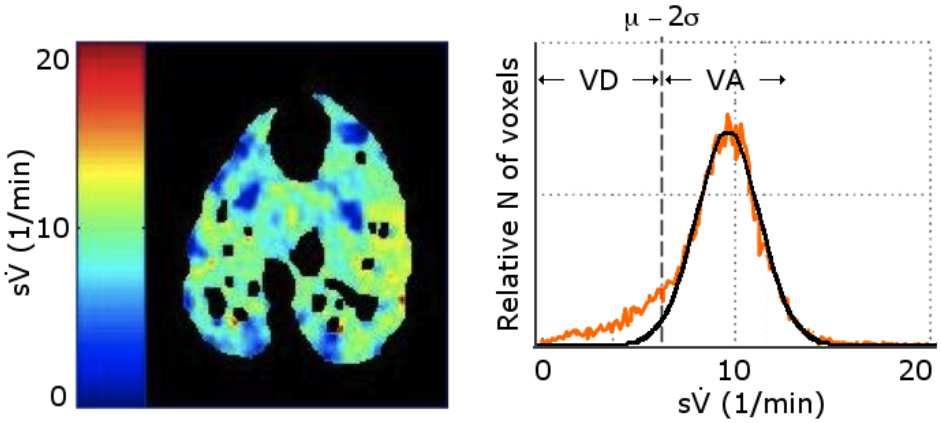


**Figure 4.8.** Log-normal fitting to a histogram of a specific ventilation ( $s\dot{V}$ ) image.

The ventilated alveolar area (VA) is defined as the area of the ventilation image where $s\dot{V}$ is greater than the median of the distribution ($\mu$) minus two standard deviations ($\sigma$), (VA: $s\dot{V} > \mu\text{-}2\sigma$). The remaining lung regions, including poorly ventilated and non-ventilated areas, are expressed as ventilation defects (VD: $s\dot{V} < \mu\text{-}2\sigma$). A similar analysis may be used in the analysis of ventilation based on a single Xe density image.

The heterogeneity of ventilation is calculated from $s\dot{V}$ ventilation or Xe density histograms as the coefficient of variation (CV) using mean value ( $\bar{x}$ )

$$CV = \frac{\sigma}{\bar{x}}. \qquad (4.10)$$

*4.4.4 Analysis of tissue images*

Airway dimensions and regional lung tissue densities are defined from the tissue density images. Cross-sectional areas (CA) of the central airways are calculated by fitting an ellipse to the lumen and determining the minor axis of the airway (Figure 4.9).

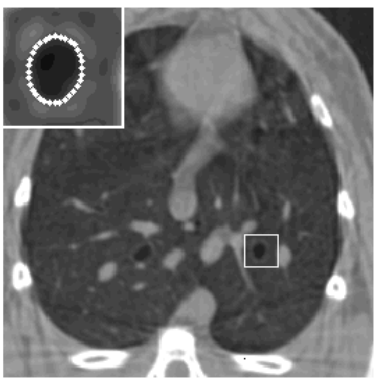

**Figure 4.9.** Tissue density image showing the analysis of central airway cross-sectional areas.

The total lung area is defined as the area within the tissue images inside the lung tissue mask, where the large airways and blood vessels are excluded.

Tissue density images can be converted into commonly used units in image processing. The unit of mass density expressed as g/ml is transformed to Hounsfield units (HU) as follows

$$HU = 1000 \times \frac{\mu_Z - \mu_{water}}{\mu_{water}}, \tag{4.11}$$

where $\mu_Z$ denotes the average linear attenuation coefficient in a voxel and $\mu_{water}$ is the linear attenuation coefficient of water, which can be derived from the mass attenuation coefficient. For calculating the total lung area -900 HU was used as a lower threshold [Vieira et al., 1999, Bayat et al., 2013].

The density of the lung tissue was defined within the lung tissue mask. Gas content defines the fraction of gas contained in the image regions corresponding to lung. Gas content can be calculated from lung tissue density, or from the ratio of the asymptotic Xe concentration during wash-in, to the Xe concentration of the inhaled gas within central airway lumens.

## *4.5 Animal experiments*

Animal care and experimental procedures were in accordance with the Guide for the Care and Use of Laboratory Animals [ILAR, 2011] and were approved by the local institutional authorities in France. Experiments were performed on healthy and ovalbumin-sensitized New Zealand male rabbits (2.5-3.0 kg).

### *4.5.1 Animal preparation and anesthesia*

Animals were anaesthetized, tracheostomized and paralyzed during imaging. Local anesthesia (5% topical lidocaine, Emla, Astra-Zeneca, Rueil, France) was used to prepare an ear vein by a catheter (22-gauge, Cathlon i.v., Ethicon, Rome, Italy) for i.v. anesthesia. For infusing drugs, for blood gas sampling ($PaCO_2$, $PaO_2$, pH) and blood pressure monitoring (Radiometer model 77, Acid Base Laboratory, Copenhagen, Denmark) a catheter (22-gauge) was inserted into the left carotid artery. Anesthesia was initiated by i.v. thiopendal sodium (25 mg/kg i.v., Nesdonal, Rhone-Poulenc- Rohrer, Paris, France) and anesthesia was maintained either by inhaled isofluraine (0,4%, Forene, Abbott, Paris, France) or i.v. Midazolam (0.2 mg/kg/h, Aguettant, Lyon, France). Animals were paralyzed by i.v. Atracurium (1.0 mg/kg/h, Tracrium, GlaxoSmithKline, Münchenbuchsee, Switzerland) or i.v. vecuronium bromide injections (1.0 mg/h, Norcuron, Organon, Puteaux, France), and tracheostomized with an endotracheal tube (no. 3 to 3.5, Portex, Berck sur Mer, France) for mechanical ventilation. The animal was immobilized in a holder in the vertical position without

disturbing the chest and diaphragm movements. The mechanical ventilation system was controlled during the experiments by the operating system. Endotracheal pressure (Ptr) and ventilatory gas flow were monitored continuously by a pressure gauge and a heated pneumotachometer (Hans Rudolph, Kansas City, MO). Signals from the monitoring probes were amplified, digitized at 1000 Hz (PowerLab, ADInstruments, Oxfordshire, UK), and recorded on a computer. Images were taken during respiratory pause to avoid lung shape and volume changes during image aquisition.

### *4.5.2 Airway challenge methods*

Methacholine (MCh) (Sigma, St. Quentin Fallavier, France) was used to induce a bronchoconstriction in the lungs. Inhaled MCh was administered using an ultrasonic nebulizer on the endotracheal tube (SAM LS2000, Villeneuve sur Lot, France) and i.v. MCh infusion was administered via an ear vein. Doses delivered varied depending on the study.

For producing reactions similar to asthma in the airways, the animals were sensitized to OVA as detailed previously [Petak et al., 2006]. Sensitization was performed using intra-peritoneal injections of a solution containing 0.1 mg of OVA (Sigma-Aldrich Chimie S.a.r.l., St. Quentin Fallavier, France) and 10 mg of aluminum hydroxide as an adjuvant (Merck KGaA, Darmstadt, Germany). The solution was administered 30 and 17 days before the imaging experiment and the animals were exposed to aerosolized OVA (10 mg/ml for 20-min) daily for 5 days prior to the experiments using an ultrasonic nebulizer (Systam LS290, Velleneuve sur Lot, France). During the experiment, i.v. injection of OVA (2.0 mg) was used to induce an allergic asthmatic reaction in sensitized animals [Article I and II].

Cigarette smoke provocation was used to investigate the combination of Mch induced bronchoconstriction and mainstream cigarette smoke. The smoke of filtered cigarettes (Marlboro; Philip Morris International, Lausanne, Switzerland) was produced by a Plexiglass chamber connected to the inspiratory branch of the ventilation circuit. The smoke, with an average yield of 0.8 mg of nicotine, 10 mg of tar, and 10 mg of CO per cigarette, as stated by the manufacturer, was diluted with air inside the smoke chamber and directed to the lungs. The animals were exposed to mainstream smoke from each of four cigarettes for 7 min.

## *4.6 Dosimetry of x-ray radiation*

The radiation dose was estimated by three different methods; by calculating the dose rate based on the beamline optics and starting from the source, by measuring the dose with a dosimeter at the focus (Figure 4.5) and by calculating the dose from measurement of the number of photons collected by the detector.

### *4.6.1 Dose from the source*

The absorbed dose ($D$) in an object can be calculated from the properties of the synchrotron radiation source and the x-ray optics of the beamline. If we assume that no energy escapes the volume of interest as high-energy electrons or x-ray bremsstrahlung, $D$ can be defined at low photon energies (34.56 keV) as the imparted energy $dE$ per unit mass element $dm$ [Graeff and Engelke, 1991]:

$$D = \frac{dE}{dm} = \Phi_0 E_\gamma \left(\frac{\mu}{\rho}\right)_{en} \tag{4.12}$$

where $\Phi_o = N_o/A$ is the photon flux on area $A$, $E_\gamma$ the photon energy, and $(\mu/\rho)_{en}$ the mass energy absorption coefficient. The dose rate at the focus, where the object is placed, is calculated from the intensity of the two x-ray beams. The absorbed power of the monochromatic synchrotron radiation beams per unit volume can be calculated from the synchrotron radiation beam power and the x-ray optics [Erola et al., 1990, Suortti et al., 1993]:

$$\frac{dP}{dV} = I\mu_{en} = \left(\frac{P}{hw}\right)\mu_{en} = \left(\frac{P_0}{hw}\right)\mu_{en}\cot\theta\int R(\theta)\,d\theta\,, \tag{4.13}$$

where $I$ is the intensity, $P_o$ is the incident power, $\mu_{en}$ is the energy absorption coefficient, $h$ is the height, $w$ is the width of the focused beam, $\theta$ is the Bragg angle and $R(\theta)$ is the reflectivity of the monochromator crystal. While the mass ($m$) is density ($\rho$) multiplied by volume ($V$), the dose rate can be calculated from the equation 4.12 using the absorbed power:

$$\frac{dD}{dt} = \frac{1}{\rho}\left(\frac{dP}{dV}\right). \tag{4.14}$$

### *4.6.2 Dose at the dosimeter*

The dose measurements were performed using standard protocols in medical x-ray imaging [ICRU, 2005, IAEA, 2007] in order to compare the dose between KES CT imaging and clinical CT imaging. A pencil-shaped ionizing chamber, introduced by Suzuki and Suzuki [1978], was chosen over thermoluminescent dosimeters for its reliability (uncertainty below 5%) reusability and acceptance for international procedures [Oliveira et al., 2011]. A 15 cm long ionization chamber (type 77336, Physikalisch-Technische Werkstätten, PTW, Freiburg, Germany) was connected to an electrometer (Unidos, PTW, Freiburg, Germany). This dosimeter integrates the air kerma ($K_a$; kinetic energy released per unit mass), which equals $D$, and yields the air kerma length product ($P_{KL}$) in mGy·cm as

$$P_{KL} = \int_L K_a(L)\,dL = K_a L\,, \tag{4.15}$$

where $L$ is the integral height of the beam. For yielding $K_a$ in mGy, $P_{KL}$ was measured free-in-air and divided by beam height at the beam focus. The dose rate in mGy/s was derived by dividing $K_a$ by the exposure time, determined by the beam shutters. The exposure time was measured by the integration time of the beam monitoring ionization chambers. The total exposure time, 3.76 s, included a ramp-up of the CT rotation motor, a full turn rotation in 2 s and a ramp-down.

The mean value of three scans for each dose value was normalized to a synchrotron storage ring current of 80 mA and corrected for temperature and pressure. The system linearity was examined by varying the incident photon flux using changeable thicknesses of Plexiglass attenuators.

Computed tomography air kerma index ($C_{K,PMMA}$), referred to in practice as the computed tomography dose index (CTDI or $C_D$) [Leizt at al., 1995], was defined in a standard tissue-equivalent 16 cm diameter polymethyl methacrylate (PMMA, $\rho = 1.19^3$ g/cm) cylinder head phantom by measuring $P_{KL}$ in the center and the periphery of the phantom. The head phantom was chosen because of the limited width of the beam.

$C_{K,PMMA}$ was derived from $P_{KL}$ in a single rotation for slice thickness $L$ [ICRU, 2005]:

$$C_{K,PMMA} = \frac{1}{L}\int_{-\infty}^{\infty} K_{a,PMMA}(z)\,dz = \frac{P_{KL,PMMA}}{L}\,. \tag{4.16}$$

For proper averaging, the ion chamber was placed sequentially at the center (c) and four holes in the periphery (p) of the standard phantom. Periphery measurements were averaged and the weighted average of the center and periphery measurements was defined as:

$$C_{K,PMMA,w} = \frac{C_{K,PMMA,c} + 2C_{K,PMMA,p}}{3}\,. \tag{4.17}$$

The volume-based index $C_{K,PMMA,vol}$, provided by commercial CT scanners, depends on the choice of imaging parameters and takes exposure variation along the z axis into account, but is independent of the scan length. When scanning the phantom without axial variation $C_{K,PMMA,vol}$ is the same as $C_{K,PMMA,w}$.

### *4.6.3 Dose at the germanium detector*

The photon flux, number of photons ($N_0$) incident on the detector per pixel, is calculated as [Elleaume et al., 2002].

$$N_0 = e^{(\mu_{Be} x_{Be})} N Q_{\min} E_p \times \frac{128}{E_\gamma (1 - e^{(-\mu_{Ge} x_{Ge})}) \bar{e} \times gain} \tag{4.18}$$

where $\mu_{Be}$ is the attenuation coefficient of beryllium and $x_{Be}$ is the thickness of the beryllium window, $N$ is the detector reading (bits) in one pixel, $Q_{min}$ is the minimum detectable charge ($2 \times 10^{-15}$C), $E_p$ ist the mean energy necessary to create an electron–hole pair in germanium (2.98 eV), $E_\gamma$ is the photon energy of the monochromatic beam (34.56 keV), $\mu_{Ge}$ is the total attenuation coefficient of germanium ($cm^{-1}$), $x_{Ge}$ is the detector thickness (0.25 cm), $\bar{e}$ is the electron charge ($1.602 \times 10^{-19}$C) and '*gain*' is the electronic gain (ranges from 1 to 128 with a factor of 2 between two consecutive gains). The first term corresponds to the detector entrance beryllium window transmission factor. The beryllium and germanium attenuation coefficients are interpolated and calculated from the charts maintained by the National Institute of Standards and Technology [NIST, 2014].

The photon fluence ($\phi_0$), for sample area $A = wh$, can be calculated as [Porra, 2006]

$$\phi_0 = \frac{\Phi_0}{dt} = \frac{N_0}{wh\ dt}, \tag{4.19}$$

where $w$ is the pixel width of the detector (0.35 mm), $h$ is the beam height (0.63 mm) and $dt$ is the integration time of one line (2.2222 ms).

If the dose is calculated at the sample position based on measurements at the detector in our setup, where the sample is 6 m from the detector, we have to take account of the difference between the pixel width, 0.35 mm at the detector, and 0.336 mm at the sample and attenuation of the air between the sample and detector.

## *4.7 Image quality*

Image quality is closely related to the dose. The lowest radiation exposure for CT image acquisition should be higher than the inherent detector noise level, and the highest exposure should not outstrip the saturation level of the detector. Thus CT images can be acquired over an extensive range of exposure levels without the consequence of over or under exposed scans. Determining the threshold levels of exposure, as a function of image quality parameters, is important when optimizing the imaging sequence for *in vivo* imaging.

### *4.7.1 Signal to noise ratio (SNR)*

The signal to noise ratio (SNR), which describes the contrast and the noise of the image, was used to evaluate the image quality as a function of air kerma $K_a$, measured free-in-air, from tissue-density and Xe-density CT *in vivo* images of the animal. The signal ($S$)

was measured within selected regions-of-interest (ROIs) in the reconstructed CT images. The standard deviation of the background signal $SD_{bg}$ was determined outside the animal. SNR was defined as:

$$SNR = \frac{S}{SD_{bg}} . \tag{4.20}$$

The Matlab (MathWorks Inc., Natick, MA, USA) programming package was used to process the images and calculations of image quality were done with ImageJ software (National Institutes of Health, USA).

### *4.7.2 Modulation transfer function (MTF)*

The modulation transfer function (MTF) was defined for describing the resolution of the imaging setup. A sharp edge phantom was imaged vertically and the edge method [Samei et al., 1998] was used for calculating the MTF. First the edge spread function (ESF) of the imaging setup, which denotes the system response to a high contrast edge, was determined from the edge transition. The line spread function (LSF) was obtained by differentiating the ESF. The MTF was defined via Fourier transformation of the LSF.

### *4.7.3 Deep dose curve*

The attenuation of tissue-equivalent PMMA was also tested with a plane parallel ionization chamber (Type 23342, Ptw-Freiburg, Freiburg, Germany) [Fiedler et al. 2004]. The attenuated dose was measured by scanning the chamber across the beam in the z direction. The scan velocity was 50 mm/s, scan time was 2 seconds and scan height was 100 mm. In the deep dose curve measurements a stack of 1 cm PMMA places were used to simulate the soft tissue. Suitability of this ionization chamber for CT measurements was investigated recently by Liebmann M et al. [2012]. The chamber was used previously in synchrotron radiation measurements by Fiedler et al. [2004].

### *4.7.4 Density measurements*

Accuracy of the density measurements was tested with five different materials including the background air. Bars of soft tissue equivalent PMMA and lung equivalent polystyrene, and syringes filled with water and Xe gas were inserted into the beam and imaged using the same parameters as in the CT lung imaging. The temperature, 24.0˚ C, and the pressure, 1001.2 mbar, at the time of the measurements were taken into account.

# 5 Results

## *5.1 Results of animal experiments*

Xe density and tissue density CT images were acquired at two or three thoracic lung levels: apical, middle and caudal. The distribution of ventilation was investigated by two methods: specific ventilation images calculated from wash-in series or from single Xe density images.

### *5.1.1 Methacholine challenge*

Effects of MCh challenge were studied in **articles I** and **III**. I.v. MCh infusion induced constriction predominantly in the central airways in both healthy and sensitized animals by decreasing the cross-sectional area (CA) calculated from the tissue density images. As well, inhaled MCh constricted conducting airways by decreasing the CA, but the increase was modest compared to the effect of i.v. MCh in healthy animals (Figure 5.1).

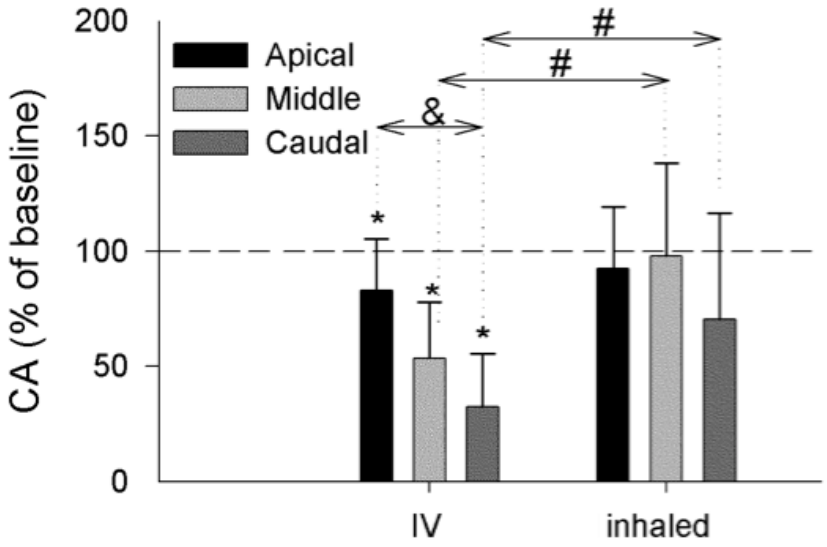


**Figure 5.1.** Cross-sectional area (CA) of central airways at three thoracic lung levels of healthy rabbits during intravenous MCh and following inhaled MCh. The results are presented as percentages of the baseline (dash line). Significance of the results was tested with ANOVA: *$p < 0.05$ versus baseline; # $p < 0.05$ versus IV; & $p < 0.05$ between axial image levels. Figure adapted from article III.

The effects of Mch on the periphery of the lungs by $s\dot{V}$ images was reported in **article I** and by Xe density images in **article III**. Inhaled Mch induced marked bronchoconstriction in peripheral airways, while the peripheral response to i.v. Mch was mild in healthy animals, which can be seen in both Xe density, acquired at 70-80% of lung filling, and $s\dot{V}$ images (Figure 5.2).

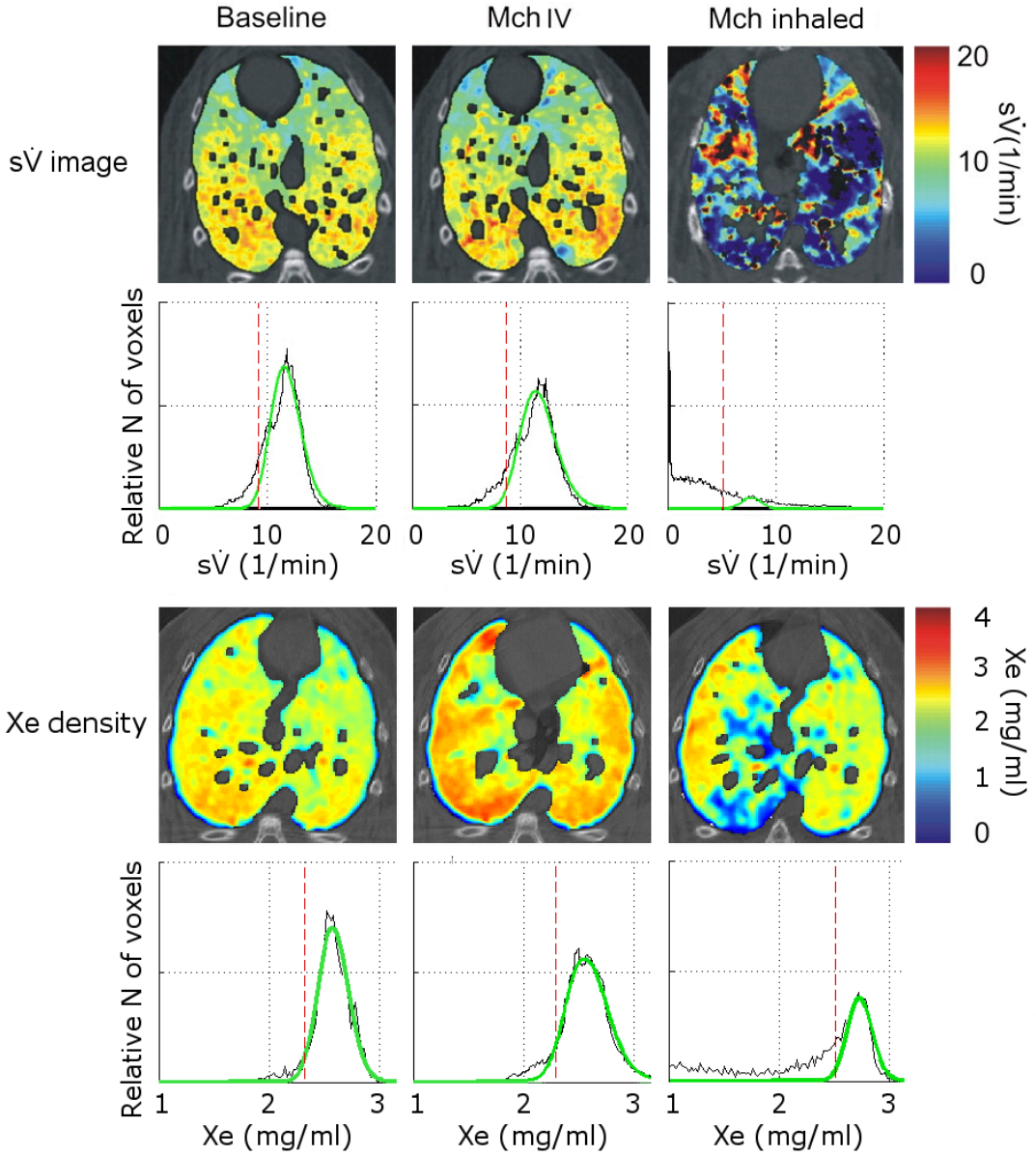


**Figure 5.2.** Xenon (Xe) density and specific ventilation ( $s\dot{V}$ ) images and histograms from two healthy rabbits at baseline, following intravenous MCh and after inhaled MCh challenge.

Reduction of well ventilated areas in the lungs and rise of heterogeneity is shown in decreased values of VA and increased values of VD. Rise of heterogeneity is evident from the decrease of coefficient variation in both Xe density and $s\dot{V}$ images.

### *5.1.2 Ovalbumin (OVA) challenge*

Effects of OVA challenge on regional ventilation was studied in **article I**. I.v. OVA challenge mildly affected the conducting airways by decreasing the CA of central

airways. Whereas the effects of i.v. MCh challenge were small, the main effect of injected OVA focused on peripheral airways by decreasing VA in sensitized rabbits. This led to severe ventilation heterogeneities detected by the $s\dot{V}$ images (Figure 5.3) and decrease of coefficient variation. Contrary to sensitized rabbits there was no effect in ovalbumin challenge in healthy rabbits.

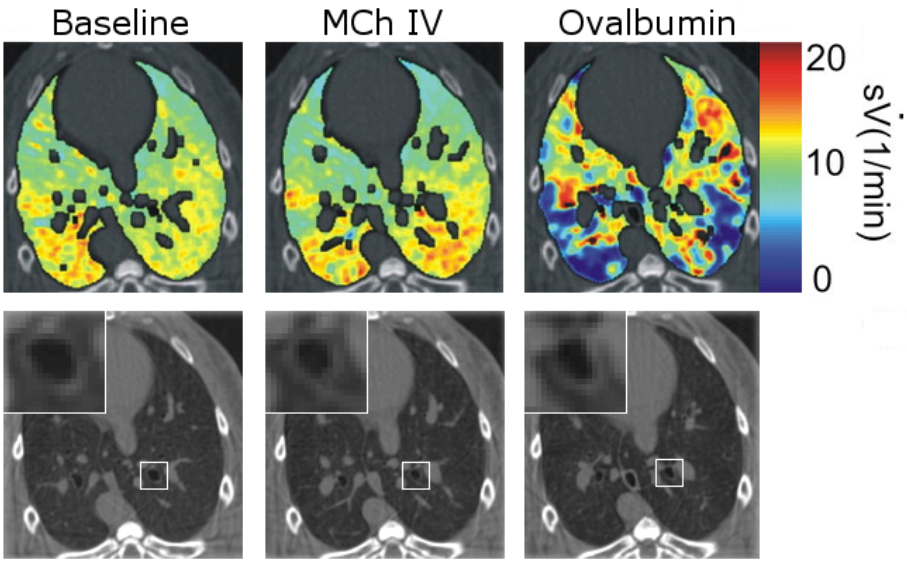


**Figure 5.3.** Specific ventilation ($s\dot{V}$) images (upper panels) and tissue density images showing the cross-section of a large airway, magnified in the upper corner (lower panels) of an ovalbumin-sensitized rabbit at the baseline, during intravenous methocholine (MCh IV) challenge, and after intravenous ovalbumin challenge.

### *5.1.3 Cigarette smoke challenge*

Acute effects of cigarette smoke on the response to MCh and OVA challenges were investigated in **article II**. We found that acute exposure to cigarette smoke inhibits the airway response to i.v. MCh challenge in central and peripheral airways in both control and ovalbumin-sensitized rabbits (Figure 5.4).

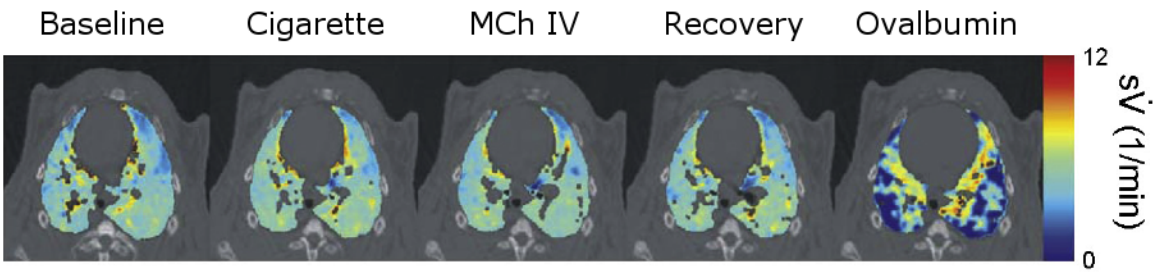


**Figure 5.4.** Specific ventilation ($s\dot{V}$) images of sensitized rabbit at baseline, following exposure to cigarette smoke, during intravenous methacholine infusion (MCh IV), upon recovery and after intravenous ovalbumin provocation. Figure adapted from article II.

The inhibition of bronchoconstriction by i.v. MCh can be seen in response of cross-sectional area of large airways (Figure 5.5).

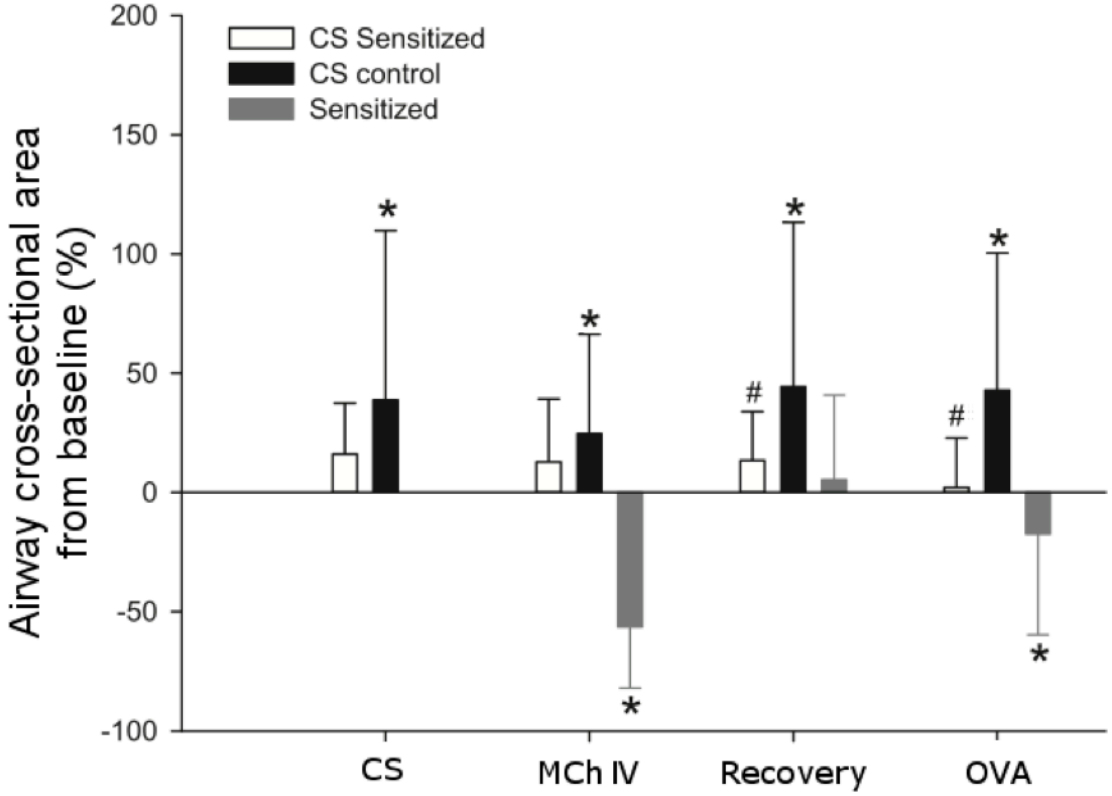


**Figure 5.5.** Changes in the cross-sectional area of large airways at the baseline, after cigarette smoke provocation (CS), during methacholine challenge (M10), following recovery and after ovalbumin challenge (OVA) in ovalbumin-sensitized rabbits with cigarette smoke provocation (CS Sensitized), without cigarette smoke provocation (Sensitized) and in healthy rabbits with cigarette smoke provocation (CS Control). Significance was tested by 2-way repeated measures by ANOVA: *$p < 0.05$ versus baseline, #$p < 0.05$ versus the cigarette smoke exposed control group. Figure adapted from article II.

The decrease of the cross-sectional area of large airways indicating bronchoconstriction was significant during in i.v. MCh challenge, as shown in **articles I** and **III**. The inhalation of cigarette smoke blunted the bronchoconstriction almost completely. A similar effect occurs also in OVA challenge with smaller impact. Although the airway response to OVA challenge was also inhibited in the central airways, cigarette smoke exposure did not blunt the allergen-induced peripheral lung response in sensitized rabbits as evidenced by heterogeneity of $s\dot{V}$ found in the functional $s\dot{V}$ images. The inhibition effect of cigarette smoke persisted in both sensitized and healthy animals, when cigarette smoke was filtered by HEPA filtering. The inhibitory effect could not be induced by inhaled NO or CO gas, which are included in cigarette smoke. In addition, cigarette smoke did not induce significant changes in lung tissue density or lung dimensions.

## *5.2 Radiation dose and image quality*

Means of determining the radiation dose and the effects on image quality were studied in **article IV**. A close agreement between the dose rates measured by the dosimeter (2.13 ± 0.24 Gy/s), the Ge detector (2.15 ± 0.24 Gy/s) and with the value calculated from the source parameters and beamline optics (1.95 ± 0.22 Gy/s) was found. The linear dependence between dose parameters $C_{K,PMMA,w}$, $P_{KL}$, and $K_a$ demonstrated the absence of beam hardening in the Plexiglass.

Figure 5.6 presents tissue density and Xe density images of rabbit lung for different Plexiglass thicknesses, which were used for measurements of image quality parameters. Results of **article IV** are summarized in following sections together with some unpublished imaging and dosimetry data.

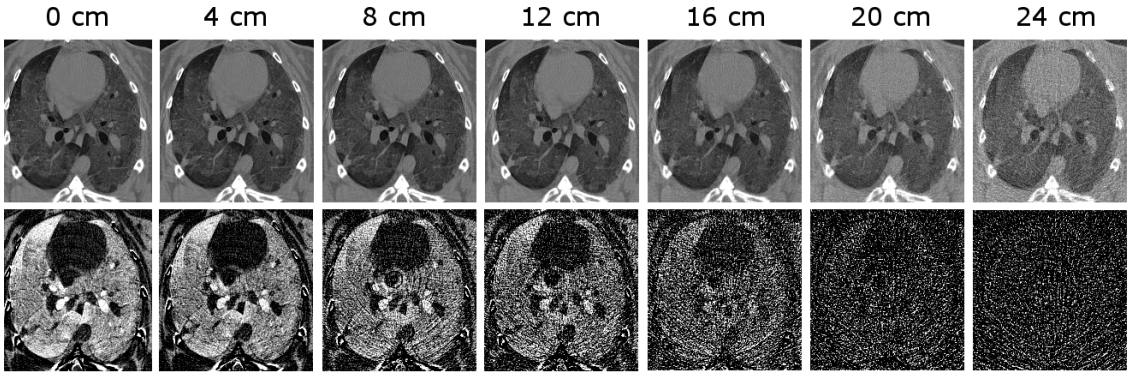


**Figure 5.6.** Tissue density (upper row) and xenon density (lower row) images of rabbit lung for different Plexiglass thicknesses with 20 % xenon concentration in the inhaled gas.

### *5.2.1 Signal to noise ratio (SNR)*

Image quality values, defined by SNR, showed a detection limit in agreement with the Rose criterion, SNR = 5 [Rose, 1973], for the bronchus lumen, lung tissue or air spaces, vessels and dorsal muscle of healthy rabbits, as a function of the radiation dose in both tissue density images and Xe density images [**article IV**]. The results show the difference for two concentrations (20% and 70%) of inhaled Xe (Figure 5.7).

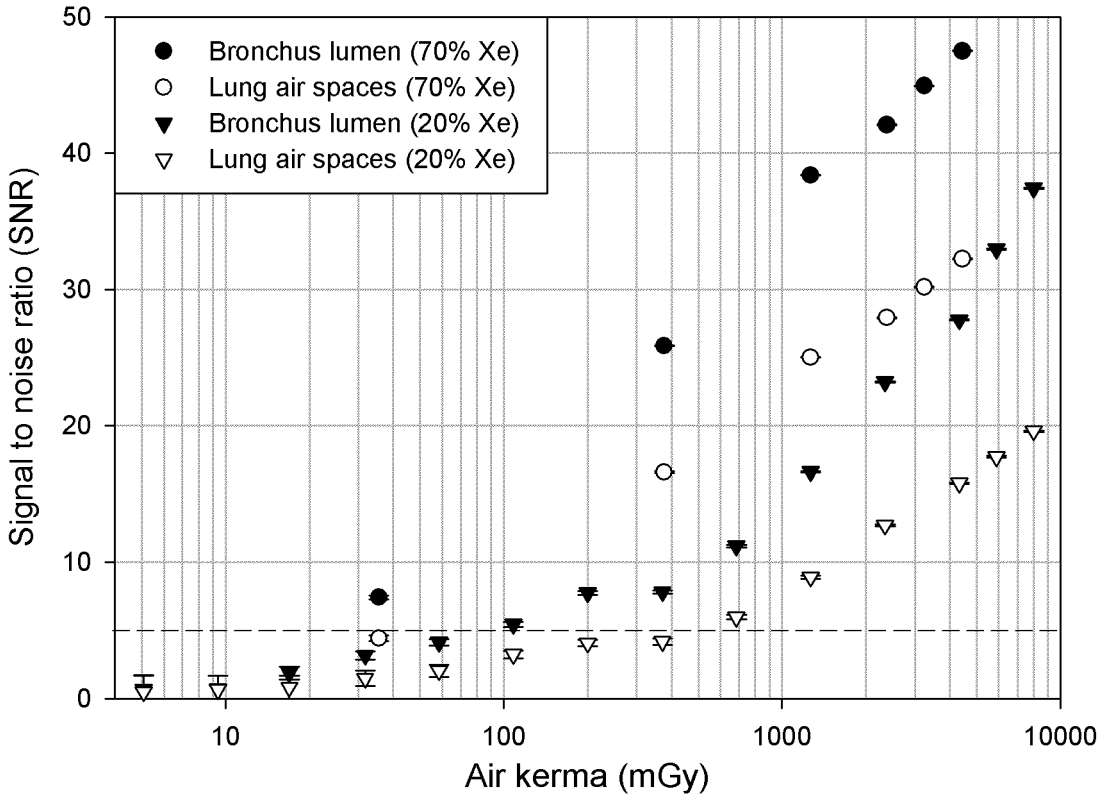


**Figure 5.7.** Signal to noise ratio (SNR) of bronchus lumen and lung air spaces as a function of air kerma ($K_a$) in rabbit lung calculated from KES CT images with 20 %, and 70% of xenon (Xe) in inhaled gas.

In light of these results, the limitations due to radiation exposure can be overcome while retaining sufficient contrast resolution for quantitative mapping of ventilation.

### *5.2.2 Modulation transfer function (MTF)*

Figure 5.8 shows the unpublished data of the MTF for synchrotron radiation based tissue images. The form of the MTF was independent of the radiation dose.

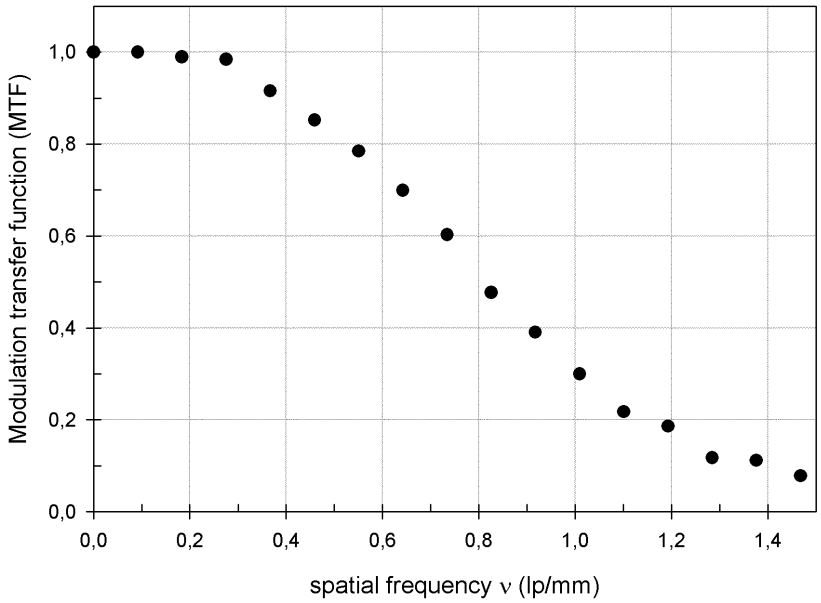


**Figure 5.8.** Modulation transfer function of tissue density images using synchrotron radiation.

### *5.2.3 Deep dose curve*

The deep dose curve is presented in figure 5.9, where the relative dose is shown as a function of PMMA thickness. The apparent non-linearity of dose for large PMMA thicknesses is probably not due to beam hardening but arises from increasing scattering to the ionization chamber.

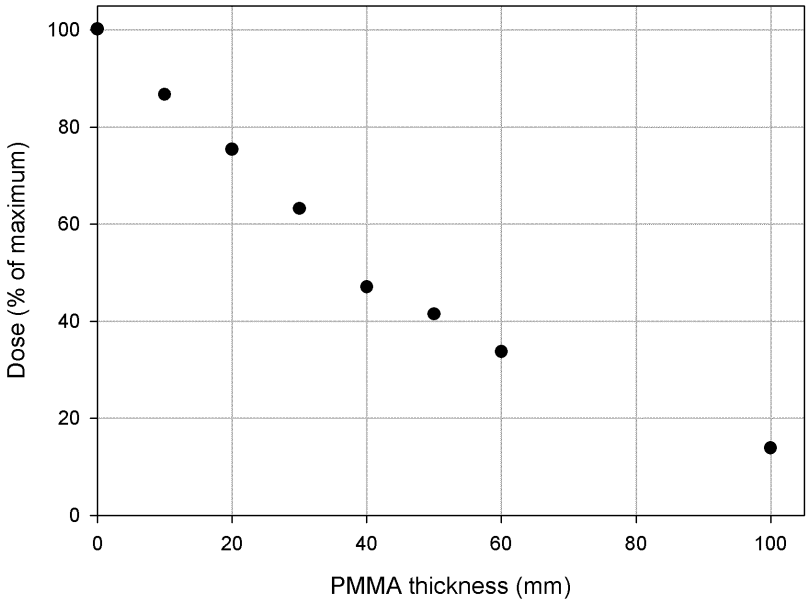


**Figure 5.9.** Relative deep dose as a function of polymethyl methacrylate (PMMA) thickness using synchrotron radiation.

### *5.2.4 Density measurements*

Contrast enhancement with 20 % Xe inhalation was 110 HU [**article IV**]. Unpublished data of density measurements show that measured densities correspond to the published references in the tissue density images. In the Xe density images all materials except Xe are subtracted away and therefore only Xe is visible. The error bars increase, when the dose is diminished. Densities of the Xe in the phantom, PMMA, polystyrene, water and air as a function of Plexiglass thickness in tissue density and Xe density images are showed in Fig. 5.10.

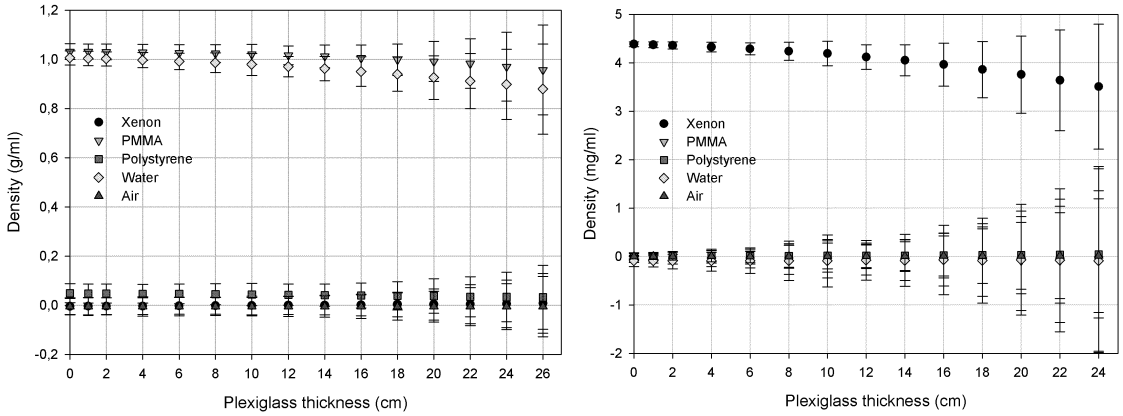


**Figure 5.10.** Density measurements of xenon phantom, polymethyl methacrylate (PMMA), polystyrene, water and air calculated from tissue density images (left) and xenon density images (right).

Densities of materials defined by these measurements without Plexiglass and reference values are listed in table 5.1.

Table 5.1. Density of materials according to the manufacturer or from encyclopedia.airliquide.com [2014] and the measured values from the tissue density images (PMMA, water, polystyrene, air) or xenon density images (Xenon).

| Material | Density (g/ml) | Measured density (g/ml) |
|---|---|---|
| Polymethyl methacrylate (PMMA) | 1.180 | 1.032±0.032 |
| Water | 1.000 | 1.006±0.029 |
| Polystyrene | 0.040 | 0.048±0.037 |
| Xenon | 0.005584 (100%) | 0.004384±0.000052* |
| Air | 0.001225 | -0.005±0.033 |

*Concentration of xenon gas was considerably lower than 100%.

# 6 Discussion

Each topic and the physiological and pathophysiological findings obtained by the KES CT method are discussed in the corresponding papers. In this section, the advantages and limitations of the methods used are discussed in relation to the results of the experiments. The possible dose reduction necessary for future human studies is also discussed. The discussion concludes with some future aspects of the KES imaging technique.

## *6.1 Advantages of K-edge subtraction CT imaging*

The K-edge subtraction CT imaging method is a quantitative method for functional lung imaging using a non-toxic contrast agent while it makes possible imaging of the structures of the lungs with high resolution. With this method it is possible to directly measure the density of the tissue as well as that of the contrast agent simultaneously, which makes this method superior to other imaging methods. In this series of study, stable Xe gas is used to study distribution of ventilation and regional lung volumes. The spatial resolution is high (voxel size 0.1 $mm^3$) and the temporal resolution has been shown to be sufficient for functional lung imaging *in vivo* (one image/s) [Bayat et al., 2008].

The regional aeration of the lungs can be evaluated from conventional synchrotron radiation CT images by segmenting the areas filled with gas [Dubsky et al., 2012]. However, the slow ventilation areas and air trapping in the peripheral airways, could not be detected in these images. Besides the measurement of the regional aeration, KES CT allows imaging the gas movements and quantification of the distribution of inhaled contrast agent, thereby allowing assessment of regional aeration, areas of slow ventilation, and air trapping in the small airways. These unique features were used in the present studies of experimental asthma, where the distribution of ventilation is typically disturbed.

There are a few other imaging techniques that are used to study the regional heterogeneity of the ventilation. While they have their own advantages compared to the KES imaging method, they have their limitations. An advantage of methods using radioactive tracers, PET [Venegas et al., 2005] and SPECT [Pellegrino et al., 2001], is the availability of the scanners and tracers, but these methods have relatively poor spatial and time resolution. While the radioactive radiation of these methods is tolerable for human studies, the images obtained are not absolutely quantitative. MRI has good spatial resolution, availability, and does not use ionizing radiation [Biederer et al., 2014], but the technique suffers from poor time resolution and contrast, artefacts and deficiency of quantification. The relatively high radiation dose, motion artefacts in serial acquisition, as well as poor quantification, limits the Xe-enhanced CT imaging [van Beek and Hoffman, 2008]. Also, the contrast enhancement is less than a half with a standard CT machine using low Xe inhalation compared to the synchrotron radiation based KES method [Chon et al., 2007]. On the other hand, the large imaging field, good

temporal resolution, and availability of instrumentation are advantages compared to the KES imaging technique. The combination of the imaging techniques (MRI-CT, PET-CT, SPECT-CT) may remove the shortcomings but the motion artefacts and registration of two image scales will cause an error in the measurements. Because the subtraction of tissue images and contrast images are taken simultaneously in the KES method, the movement artefacts caused by temporal subtraction can be avoided.

Image quality of KES CT is related to the delivered radiation dose as shown in the present study. The spatial resolution is superior in the KES CT method compared to most of the non-invasive functional lung imaging methods. The signal contrast of the bronchus is improved by contrast agents so that functional imaging can be carried out within reasonable dose limits with an adequate signal to noise ratio.

## *6.2 Limitations of K-edge subtraction CT imaging*

The limitation of this technique involves the use of ionizing radiation. When the image quality is optimized, the dose is indisputably high and cannot be applied to human studies. However the radiation dose can be lowered by several means to meet the clinically acceptable doses.

The detector limits the spatial resolution of the KES method. In this series of study we used a Ge detector with spatial resolution of 0.35 mm and slice thickness of 0.63 mm. With this resolution it is possible to detect the 8th generation (1 mm) of the rabbits airways [Ramchandani et al., 2000]. In preliminary data using a 2D FReLoN (Fast Read-out Low Noise) detector with a pixel size of 50 μm [Bravin et al., 2003] we have managed visualization structures as far as at the alveoli level, a diameter of 100 μm in human [Ochs et al., 2004]. By upgrading the monochromator and the detector we could assess better spatial and temporal resolution, and therefore achieve higher image quality.

Other limitations of the imaging setup are the dimensions and lack of movability of the x-ray beam. The beam is planar and stationary, therefore the imaged object has to be moved vertically and rotated (CT imaging) for image acquisition, which limits the temporal resolution of imaging. The feasibility of Xe KES planar imaging has already been demonstrated in humans [Giacomini et al., 1998]. Besides the beam being stationary, its dimensions are limited. Imaging an object that is wider than the beam complicates the reconstruction process for CT images but is still possible.

The availability of the synchrotron x-ray source sets a limit to the extent of the use of this unique technique. The requirement of the intense flux of the beam is the main limitation for applications using conventional sources. At present, only the synchrotrons can deliver sufficient photon flux that can be used for KES CT imaging with the time resolution required for ventilation imaging.

## *6.3 Radiation dose reduction*

The main disadvantage of KES imaging technique for human imaging is the high radiation dose. Therefore we have to develop new methods for image acquiring and processing that provide sufficient image quality at clinically acceptable low radiation dose. Another issue dealing with imaging of human lung is the thickness of the thorax. For human thorax the attenuation factor is about 20 times larger compared to rabbit lung.

Besides the imaging setup and protocols, the reconstruction and analysis routines for functional images are necessary to develop for future human studies. Specific ventilation images calculated from a multiple image wash-in series may be replaced by taking only one image at the right time [Porra et al., 2009]. Also, by controlling the exposure time with shutter action [Renier et al., 2005], the radiation dose can be reduced substantially. Replacing the filtered back projection (FBP) reconstruction algorithm presently used by iterative reconstruction methods may allow the reduction of the dose by over 50% in chest CT [Hou et al., 2012, Yamada et al., 2012, Kalra et al., 2013, Mueck et al., 2013]. Our preliminary results show that by reconstructing images from fewer projections using a multiplicative algebraic algorithm it is possible to create Xe density images with considerably reduced radiation dose. We have estimated that by optimizing the imaging sequence of the current setup and reconstruction algorithms, the radiation dose could be reduced to clinically acceptable values.

## *6.4 Future aspects*

KES imaging with synchrotron radiation enables the investigation of a wide range of pulmonary conditions, not only ventilation based but also structure related disorders. These new analyzing methods provide more information of the disturbances of regional ventilation and alterations in the airways and lung tissue. Novel parameters and calculation methods are being studied for getting more information from the images and achieving better image quality with less radiation dose.

The present work demonstrates that the radiation dose may be reduced without compromising the image quality, so that human studies are possible using KES CT imaging. The method is suitable for experimental studies for investigating the mechanisms of asthma and other lung diseases, which may induce heterogeneity of ventilation and lung volumes. At the moment, it would not be suitable for diagnostic use in humans due to the limited availability of synchrotron radiation. Safety of the synchrotron radiation imaging system has been already approved in human coronary angiography studies [Elleaume et al., 2009b].

Since the intense radiation is nowadays only provided by a few relatively inaccessible synchrotron radiation facilities based on large high-energy storage rings, the interest in synchrotron applications has speeded up the development of compact synchrotron radiation sources. Compact, room sized synchrotron radiation sources will facilitate

future development of medical KES CT imaging not only for research purposes but also at the hospitals for clinical applications. Preliminary information indicates that x-ray beams from an existing compact synchrotron radiation source [Loewen, 2003, Achterhold et al., 2013] may be suitable for the KES imaging method using Xe as a contrast agent.

With a combination of two contrast agents with two different K-edges we have imaged two targets indicating gas and blood volume within the lung successively with a short time internal, which brings a new perspective to the lung function imaging. Specifically, using xenon for lung ventilation imaging and iodine for blood imaging, quantitative calculation of the ratio of ventilation and perfusion can be achieved [Suhonen et al., 2008, Guilbart et al., 2012]. With this technique we may be able to define quantitatively $\dot{V}/\dot{Q}$ mismatch, which is linked to the reasons for hypoxemia in different pulmonary diseases.

# 7 Conclusions

In this thesis methods of analyzing K-edge subtraction imaging were developed for the visualization of the quantitative distribution of regional lung ventilation and volumes of the lung. KES CT imaging showed the regional differences in ventilation during airway challenge by two Xe based methods: first, with a high sensitivity method, specific ventilation imaging based on wash-in series of images, and second, with less delivered radiation dose, single Xe ventilation imaging. For both methods several analyzing methods and parameters were developed to show the regional effects on the ventilation and on the anatomic structures in airway challenges.

We demonstrated with KES CT method that the bronchoconstriction primarily in the large airways in smooth muscle provocation with methacholine in healthy and ovalbumin sensitized (asthmatic) rabbits, and ventilation heterogeneity of peripheral airways in allergen provocation with ovalbumin in ovalbumin sensitized rabbits. Inhaled cigarette smoke was found to inhibit the bronchoconstriction caused by methacholine and ovalbumin.

Theoretical and measured radiation dose rate values showed a good agreement. We found several ways to reduce the radiation dose by optimizing the imaging setup and sequences.

The image quality was clearly dependent of the radiation dose for *in vivo* rabbit lung with and without a contrast agent (Xe). We evaluated the radiation dose for the detectability threshold according to the Rose criterion for both tissue and Xe density images.

# Author's contribution

**I** Bayat, S., **Strengell, S.**, Porra, L., Janosi, T., Petak, F., Suhonen, H., Suortti, P., Hantos, Z., Sovijärvi, A. & Habre, W. (2009). Methacholine and ovalbumin challenges assessed by forced oscillations and synchrotron lung imaging. *American Journal of Respiratory and Critical Care Medicine*, 180(4):296-303.

In this publication we studied the bronchoconstriction caused by i.v. MCh and ovalbumin in healthy and ovalbumin-sensitized rabbits. In this study we combined FOT with our setup and compared the acquired results to the newly developed imaging parameters of ventilation heterogeneity. The respondent took part in performing the experiments and co-developed and performed data analysis and participated in the writing.

**II** Porra, L., Petak, F., **Strengell, S.**, Neitola, K., Janosi, T. Z., Suhonen, H., Suortti P., Sovijärvi, A. R. A., Habre, W. & Bayat, S. (2010). Acute cigarette smoke inhalation blunts lung responsiveness to methacholine and allergen in rabbit: differentiation of central and peripheral effects. *American Journal of Physiology: Lung Cellular and Molecular Physiology,* 299(2):242-251.

In this article the effects of the combination of cigarette smoke and i.v. MCh was investigated in the lungs of healthy and ovalbumin-sensitized rabbits. Calculations of lung tissue density, total lung area and gas content were developed. The respondent took part in planning the experiments, performing the experiments, writing, and the data analysis.

**III** **Strengell, S.**, Porra, L., Sovijärvi, A., Suhonen, H., Suortti, P. & Bayat, S. (2013). Differences in the pattern of bronchoconstriction induced by intravenous and inhaled methacholine in rabbit. *Respiratory Physiology & Neurobiology*, 189(3):465-472.

This article tackles the problem of the differences in the airway responses of the administration routes of MCh and how to show these differences quantitatively. For this article we processed the imaging parameters to show the affected areas clearly. The respondent took part in performing the experiment, and was responsible for performing data analysis and was responsible for an essential part of the writing.

**IV** **Strengell, S.**, Keyriläinen, J., Suortti, P., Bayat, S., Sovijärvi, ARA., Porra, L. (2014). Radiation dose and image quality in K-edge subtraction CT of lungs *in vivo*. *Journal of Synchrotron Radiation, in press, 21(6).*

This article determines the levels of radiation dose of KES CT imaging and compares the doses to the quality of the image. The respondent was responsible for planning and performing the experiments, developing and performing data analysis and writing.

# References

Achterhold K, Bech M, Schleede S, Potdevin G, Ruth R, Loewen R, Pfeiffer F. (2013). Monochromatic computed tomography with a compact laser-driven X-ray source. *Sci Rep.,* 3:1313.

Albert, M. S., Cates, G. D., Driehuys, B., Happer, W., Saam, B., Springer, C. S. Jr, Wishnia, A. (1994). Biological magnetic resonance imaging using laser-polarized 129Xe. *Nature,* 370:199–201.

Ameredes, B. T., (2004). Cardiac activity during airway resistance alterations with intravenous and inhaled methacholine. *Respir. Physiol. Neurobiol.,* 139(3), 281-92.

Avrin, D. E., Macovski, A., Zatz, L. E. (1978). Clinical application of Compton and photo-electric reconstruction in computed tomography: preliminary results. *Invest. Radiol.,* 13:217–222.

Badea, C. T., Johnston, S. M., Qi, Y., Johnson, G. A. (2011). 4D micro-CT for cardiac and perfusion applications with view under sampling. *Phys. Med. Biol.* 56(11):3351-69.

Bayat, S., Le Duc, G., Porra, L., Berruyer, G., Nemoz, C., Monfraix, S., Fiedler, S., Thomlinson, W., Suortti, P., Standertskjöld-Nordenstam, C.G., and Sovijärvi, A. (2001). Quantitative functional lung imaging with synchrotron radiation using inhaled xenon as contrast agent. *Phys. Med. Biol.*, 46(12):3287-3299

Bayat, S., Porra, L., Suhonen, H., Nemoz, C., Suortti, P. & Sovijärvi, A. (2006). Differences in the time cource of proximal and distal airway response to inhaled histamine studied by synchrotron radiation CT. *Journal of Applied Physiology,* 100(6):1964-1973.

Bayat, S., Porra, L., Suhonen, H., Janosi, T., Strengell, S., Habre, W., Petak, F., Hantos, Z., Suortti, P., and Sovijärvi, A. (2008). Imaging of lung function using synchrotron radiation computed tomography: what s new? *European Journal of Radiology*, 68S(3):S78-S83.

Bayat, S., Porra, L., Albu, G., Suhonen, H., Strengell, S., Suortti, P., Sovijärvi, A., Petak, F. & Habre, W. (2013). Effect of Positive End-expiratory Pressure on Regional Ventilation Distribution during Mechanical Ventilation after Surfactant Depletion. *Anesthesiology*, 119(1):89-100.

van Beek, E.J., Hoffman, E.A. (2008). Functional imaging: CT and MRI. *Clin. Chest. Med.* 29(1):195-216, Review.

Biederer J, Heussel CP, Puderbach M, Wielpuetz MO. (2014). Functional magnetic resonance imaging of the lung. Semin. Respir. Crit. Care Med., 35(1):74-82.

Bracewell, R. N., and Riddle, A. C. (1967). Inversion of fan beam scans in radio astronomy. *The Astrophysical Journal,* 150:427-434.

Bravin, A., Fiedler, S., Coan, P., Labiche, J.-C., Ponchut, C., Peterzol, A., and Thomlinson, W. (2003). Comparison between a position sensitive germanium detector and a taper optics CCD "FRELON" camera for diffraction enhanced imaging. *Nucl. Instrum. Methods Phys.,* Res. A 510 35-40.

Chae, E. J., Seo, J. B., Goo, H. W., Kim, N., Song, K. S., Lee, S.D., Hong, S. J., Krauss, B. (2008). Xenon ventilation CT with a dual-energy technique of dual-source CT: initial experience. *Radiology.* 248(2):615-24.

Chae, E. J., Seo, J. B., Lee, J., Kim, N., Goo, H. W., Lee, H. J., Lee, C. W., Ra, S. W., Oh, Y. M., Cho, Y. S. (2010). Xenon ventilation imaging using dual-energy computed tomography in asthmatics: initial experience. *Invest. Radiol.* 45(6):354-61.

Chon, D., Beck, K. C., Simon, B. A., Shikata, H., Saba, O. I., Hoffman, E. A. (2007). Effect of low-xenon and krypton supplementation on signal/noise of regional CT-based ventilation measurements. *J. Appl. Physiol. (1985)*. 102(4):1535-44.

Costella, S., Kirby, M., Maksym, G. N., McCormack, D. G., Paterson, N. A., Parraga, G. (2012). Regional pulmonary response to a methacholine challenge using hyperpolarized (3)He magnetic resonance imaging. *Respirology.* 17(8):1237-46.

Crapo, R.O., Casaburi, R., Coates, A.L., Enright, P.L., Hankinson, J.L., Irvin, C.G., MacIntyre, N.R., McKay, R.T., Wanger, J.S., Anderson, S.D., Cockcroft, D.W., Fish, J.E., Sterk, P.J. (2000). Guidelines for methacholine and exercise challenge testing-1999. This official statement of the American Thoracic Society was adopted by the ATS Board of Directors, July 1999. *Am. J. Respir. Crit. Care Med.* 161(1):309-29.

Cullity, B.D. (1987). Elements of x-ray diffraction. Addison-Wesley, 2nd Edition.

Dix, W. R. Intravenous coronary angiography with synchrotron radiation. *Prog. Biophys. Mol. Biol.,* 1995;63(2):159-91. Review.

Driehuys, B., Walker, J., Pollaro, J., Cofer, G.P., Mistry, N., Schwartz, D., Johnson, G.A. (2007). 3He MRI in mouse models of asthma. *Magn. Reson. Med.,* 58(5):893-900.

Dubsky, S., Hooper, S. B., Siu, K. K., Fouras, A. (2012). Synchrotron-based dynamic computed tomography of tissue motion for regional lung function measurement. *J. R. Soc. Interface*, 9(74):2213-2224.

Edelman, R. R., Hatabu, H., Tadamur, E., Li, W., Prasad, P. V. (1996). Noninvasive assessment of regional ventilation in the human lung using oxygen-enhanced magnetic resonance imaging. *Nat. Med.,* 2:1236–1239.

Elleaume, H., Charvet, A. M., Berkvens, P., Berruyer, G., Brochard, T., Dabin, Y., Dominguez, M. C., Draperi, A., Fiedler, S., Goujon, G., Le Duc, G., Mattenet, M., Nemoz, C., Perez, M., Renier, M., Schulze, C., Spanne, P., Suortti, P., Thomlinson, W., Esteve, F., Bertrand, B., and Le Bas, J. F. (1999). Instrumentation of the ESRF Medical Imaging Facility, *Nucl. Instrum. Methods Phys.,* Res. A 428:513-527.

Elleaume, H., Charvet, A.M., Le Duc, G., Estève, F., Bertrand, B., Corde, S., Farion, R., Lefaix, J.L., Leplat, J.J., Berkvens, P., Berruyer, G., Brochard, T., Dabin, Y., Draperi, A., Fiedler, S., Nemoz, C., Perez, M., Renier, M., Suortti, P., Thomlinson, W., Le Bas, J.F. (2000a). In vivo K-edge imaging with synchrotron radiation. *Cell. Mol. Biol. (Noisy-le-grand),* 46(6):1065-75.

Elleaume, H., Fiedler, S., Estève, F., Bertrand, B., Charvet, A.M., Berkvens, P., Berruyer, G., Brochard, T., Le Duc, G., Nemoz, C., Renier, M., Suortti, P., Thomlinson, W., Le Bas, JF. (2000b). First human transvenous coronary angiography at the European Synchrotron Radiation Facility. *Phys. Med. Biol.,* 45(9):L39-43.

Elleaume, H., Charvet, A. M., Corde, S., Estève, F., Le Bas, J. F. (2002). Performance of computed tomography for contrast agent concentration measurements with monochromatic x-ray beams: comparison of K-edge versus temporal subtraction. *Phys. Med. Biol.,* 47(18) 3369-85.

Encyclopedia.airliquide.com/Encyclopedia.asp (2014)

Erola, E., Eteläniemi, V., Suortti, P., Pattison, P., Thomlinson, W. (1990). X-ray reflectivity of bent perfect crystals in Bragg and Laue geometry. *J. Appl. Cryst.,* 23:35-42.

Eurostat. (2014). “Causes of death statistics" - Statistics Explained. *<http://epp.eurostat.ec.europa.eu/statistics_explained/index.php/Causes_of_death_statistics>*

Fain, S. B., Korosec, F. R., Holmes, J. H., O'Halloran, R., Sorkness, R. L., Grist, T. M. (2007). Functional lung imaging using hyperpolarized gas MRI. *J. Magn. Reson. Imaging.* 25(5):910-23. Review.

Farah, C. S., King, G. G., Brown, N. J. Downie, S. R., Kermode, J. A., Hardaker, K. M., Peters, M. J., Berend, N., Salome, C. M. (2011). The role of the small airways in the clinical expression of asthma in adults. *J. Allergy Clin. Immunol.,*129:381–7.

Fiedler, S., Bravin, A., Keyriläinen, J., Fernández, M., Suortti, P., Thomlinson, W., Tenhunen, M., Virkkunen, P., Karjalainen-Lindsberg, M. (2004). Imaging lobular breast carcinoma: comparison of synchrotron radiation DEI-CT technique with clinical CT, mammography and histology. *Phys. Med. Biol.,* 49(2):175-88.

Fornaro, J., Leschka, S., Hibbeln, D., Butler, A., Anderson, N., Pache, G., Scheffel, H., Wildermuth, S., Alkadhi, H., Stolzmann, P. (2011). Dual- and multi-energy CT: approach to functional imaging. *Insights Imaging,* 2(2):149-159.

Giacomini, J.C., Gordon, H., O'Neil, R., Van Kessel, A., Cason, B., Chapman, D., Lavendar, W., Gmur, N., Menk, R., Thomlinson, W., Zhong, Z., Rubenstein, E. (1998). Bronchial imaging in humans using xenon K-edge dichromography. *Nuclear Instruments and Methods in Physics Research*, A 406:473-478.

Graeff, W. and Engelke, K. (1991). Handbook on Synchrotron Radiation. vol 4 ed S Ebashi, M Koch and E Rubenstein, *Amsterdam: Elsevier*, 361-405

Guerrero, T., Sanders, K., Castillo, E., Zhang, Y., Bidaut, L., Pan, T., Komaki, R. (2006). Dynamic ventilation imaging from four-dimensional computed tomography. *Phys. Med. Biol*., 51(4):777-91.

Guilbart, M., Porra, L., Strengell, S., Sovijärvi, A., Suortti, P., Bayat, S. (2012). Quasi-simultaneous in-vivo synchrotron imaging of regional ventilation and blood volume distributions after methacholine provocation in rabbit. *Fundamental & Clinical Pharmacology,* 26:Supplement s1.

Gur, D., Drayer, B.P., Borovetz, H.S., Griffith, B.P., Hardesty, R.L., Wolfson, S.K. (1979). Dynamic computed tomography of the lung: regional ventilation measurements. *J. Comput. Assist. Tomogr.,* 3(6):749-53.

Habre, W., Jánosi, T. Z., Fontao, F., Meyers, C., Albu, G., Pache, J.C., Peták, F. (2010). Mechanisms for lung function impairment and airway hyperresponsiveness following chronic hypoxia in rats. *Am. J. Physiol. Lung Cell. Mol. Physiol.,* 298(4):L607-14.

Hou, Y., Xu, S., Guo, W., Vembar, M., Guo, Q. (2012). The optimal dose reduction level using iterative reconstruction with prospective ECG-triggered coronary CTA using 256-slice MDCT. *Eur. J. Radiol.,* 81(12):3905-11.

Huda, W. (2007). Radiation Doses and Risks in Chest Computed Tomography Examinations. *Proceedings of the American Thoracic Society*, 4(4):316-320.

IAEA (International Atomic Energy Agency) (2007). Dosimetry in Diagnostic Radiology: An International Code of Practice. *Technical Report Series No. 457*. (Vienna: International Atomic Energy Agency).

ICRU (International Commission on Radiation Units & Measurements) (2005). Patient Dosimetry for X-Rays used in Medical Imaging. *ICRU Report 74*. (Bethesda: International Commission on Radiation Units and Measurements).

ILAR (Institute for Laboratory Animal Research). (2011). Guide for the Care and Use of Laboratory Animals (Washington, DC: National Academies Press).

Jacobson, B. (1953). Dichromatic absorption radiography; dichromography. *Acta radiol.,* 39(6):437-52.

Juniper, E. F., Frith, P. A., Hargreave, F. E. (1981). Airway responsiveness to histamine and methacholine: relationship to minimum treatment to control symptoms of asthma. *Thorax,* 36:575–579.

Juusela, M., Pallasaho, P., Rönmark, E., Sarna, S., Sovijärvi, A., Lundbäck, B. (2013). Dose-dependent association of smoking and bronchial hyperresponsiveness. *Eur. Respir. J.*, 42(6):1503-12.

Kalra, M. K., Woisetschläger, M., Dahlström, N., Singh, S., Digumarthy, S., Do, S., Pien, H., Quick, P., Schmidt, B., Sedlmair, M., Shepard, J. A., Persson, A. (2013). Sinogram-affirmed iterative reconstruction of low-dose chest CT: effect on image quality and radiation dose. *Am. J. Roentgenol.,* 201(2):W235-44.

Keir, S., Page, C. (2008). The rabbit as a model to study asthma and other lung diseases. *Pulm. Pharmacol. Ther.,* 21(5):721-30. Review.

King, G. G., Carroll, J. D., Müller, N. L., Whittall, K. P., Gao, M., Nakano, Y., Paré, P. D. (2004). Heterogeneity of narrowing in normal and asthmatic airways measured by HRCT. *Eur. Respir. J.* 24: 211–8.

Krill, C. E., Haberkorn, R., Birringer, R. (2000). Handbook of Nanostructured Materials and Nanotechnology. Edited by Hari Singh Nalwa, *Academic Press, San Diego,* Vol 2:183.

Kruger, R.A., Mistretta, C.A., Crummy, A.B., Sackett, J.F., Goodsitt, M.M., Riederer, S.J., Houk, T.L., Shaw, C.G., Fleming, D. (1977). Digital K-edge subtraction radiography. *Radiology,* 125(1):243-5.

Kuethe, D.O., Caprihan, A., Gach, H.M., Lowe, I.J., Fukushima, E. (2000). Imaging obstructed ventilation with NMR using inert fluorinated gases. *J. Appl. Physiol. (1985),* 88(6):2279-86.

Le Duc, G., Corde, S., Elleaume, H., Estève, F., Charvet, A.M., Brochard, T., Fiedler, S., Collomb, A., Le Bas, J.F. (2000). Feasibility of synchrotron radiation computed tomography on rats bearing glioma after iodine or gadolinium injection. Jeune Equipe RSRM-UJF. *Eur. Radiol.,* 10(9):1487-92.

Lehmann, L.A., Alvarez, R.E., Macovski, A., Brody, W.R., Pelc, N.J., Riederer, S.J., Hall, A.L. (1981). Generalized image combinations in dual KVP digital radiography. *Med Phys.,* 8(5):659-67.

Leitz, W., Axelsson, B., Szendro, G. (1995). Computed tomography dose assessment — a practical approach. *Radiat. Prot. Dosim*., 57:377–380.

Levin, D.L., Chen, Q., Zhang, M., Edelman, R.R., Hatabu, H. (2001). Evaluation of regional pulmonary perfusion using ultrafast magnetic resonance imaging. *Magn. Reson. Med.,* 46(1):166-71.

Ley-Zaporozhan, J., Ley, S., Kauczor, H. U. (2008). Morphological and functional imaging in COPD with CT and MRI: present and future. *Eur Radiol.* 18(3):510-21.

Liebmann, M., Poppe, B., von Boetticher, H. (2012) SU-E-I-107: Suitability of Various Radiation Detectors Used in Radiation Therapy for X-Ray Dosimetry in Computed Tomography. *Med. Phys.,* 39(6):3649-50.

Loewen, R. J. (2003). A compact light source : Design and technical feasibility study of a LASER-electron storage ring X-ray source. Ph.D. thesis, Stanford University.

Majumdar, A., Alencar, A. M., Buldyrev, S. V., Hantos, Z., Lutchen, K. R., Stanley, H. E., and Suki, B. (2005). Relating airway diameter distributions to regular branching asymmetry in the lung. *Phys. rev. Lett.,* 95:168101.

Marcucci, C., Nyhan, D., Simon, B.A. (2001). Distribution of pulmonary ventilation using Xe enhanced computed tomography in prone and supine dogs. *J. Appl. Physiol.* (1985), 90(2):421-30.

Martin, T. R., Gerard, N. P., Galli, S. J., Drazen, J. M., (1988). Pulmonary responses to bronchodilator agonists in the mouse. *J. Appl. Physiol.,* 64(6), 2318–2323.

Middleton, H., Black, R. D., Saam, B., Cates, G. D., Cofer, G. P., Guenther, R. (1995). MR imaging with hyperpolarized He-3 gas. *Magn. Reson. Med.,* 33:271–275.

Mistry, N.N., Thomas, A., Kaushik, S.S., Johnson, G.A., Driehuys, B. (2010). Quantitative analysis of hyperpolarized 3He ventilation changes in mice challenged with methacholine. *Magn. Reson. Med.,* 63(3):658-66.

Monfraix, S., Bayat, S., Porra, L., Berruyer, G., Nemoz, C., Thomlinson, W., Suortti, P. & Sovijärvi, A. (2005). Quantitative measurement of regional lung gas volume by synchrotron radiation computed tomography. *Phys. Med. Biol.,* 50(1):1-11.

Mueck, F. G., Michael, L., Deak, Z., Scherr, M. K., Maxien, D., Geyer, L. L., Reiser, M., Wirth, S. (2013). Upgrade to iterative image reconstruction (IR) in MDCT imaging: a clinical study for detailed parameter optimization beyond vendor recommendations using the adaptive statistical iterative reconstruction environment (ASIR) Part2: The chest. *Rofo,* 185(7):644-54.

Nagase, T., Moretto, A., Ludwig, M.S. (1994). Airway and tissue behavior during induced constriction in rats: intravenous vs. aerosol administration. *J. Appl. Physiol. (1985),* 76(2):830-8.

NIST (National Institute of Standards and Technology) 2014 Physical Reference Data (Gaithersburg, MD: NIST) *http://physics.nist.gov/PhysRefData.*

Ochs, M., Nyengaard, J. R., Jung, A., Knudsen, L., Voigt, M., Wahlers, T., Richter, J., Gundersen, H. J. (2004). The number ofa alveoli in the human lung. *Am. J. Respir. Crit. Care Med.,* 169(1):120-4.

Ohno, Y., Koyama, H., Matsumoto, K. Onishi Y, Nogami M, Takenaka D, Matsumoto S, Sugimura K. (2011). Oxygen-enhanced MRI vs. quantitatively assessed thin-section CT: pulmonary functional loss assessment and clinical stage classification of asthmatics. *Eur. J. Radiol.,* 77: 85–91.

Oliveira, B. B., Mourão, A. P., DaSilva, T. A. (2011). Kerma profile measurements in CT chest scans: a comparison of methodologies. *World Acad. Sci. Eng. Technol.* 80, 88–91.

Pallasaho P, Juusela M, Lindqvist A, Sovijärvi A, Lundbäck B, Rönmark E. (2011). Allergic rhinoconjunctivitis doubles the risk for incident asthma--results from a population study in Helsinki, Finland. *Respir. Med.,* 105(10):1449-56.

Pellegrino, R., Violante, B., Selleri, R., Brusasco, V. (1994). Changes in residual volume during induced bronchoconstriction in healthy and asthmatic subjects. *Am. J. Respir. Crit. Care Med.,* 150(2):363-8.

Pellegrino, R., Biggi, A., Papaleo, A., Camuzzini, G., Rodarte, J. R., Brusasco, V. (2001). Regional expiratory flow limitation studied with Technegas in asthma. *J. Appl. Physiol.,* 91: 2190–8.

Peták, F., Hantos, Z., Adamicza, A., Asztalos, T., Sly, P.D. (1997). Methacholine-induced bronchoconstriction in rats: effects of intravenous vs. aerosol delivery. *J. Appl. Physiol. (1985),* 82(5):1479-87.

Peták, F., Czövek, D., Novák, Z. (2012). Spirometry and forced oscillations in the detection of airway hyperreactivity in asthmatic children. *Pediatr. Pulmonol.* 47(10):956-65.

Peták, F., Hantos, Z., Adamicza, A., Gálity, H., Habre, W. (2006). Development of bronchoconstriction after administration of muscle relaxants in rabbits with normal or hyperreactive airways. *Anesth. Analg.* 103(1):103-9.

Petersson, J., Sánchez-Crespo, A., Larsson, S.A., Mure, M. (2007). Physiological imaging of the lung: single-photon-emission computed tomography (SPECT). *J. Appl. Physiol. (1985),* 102(1):468-76. Review.

Piirilä, P. L., Hodgson, U., Wuorimaa, T., Smith, H-J., Sovijärvi, A. R. (2014). Thoracic gas compression during forced expiratory in patients with emphysema interstitial lung disease and obesity. *BMC Pulm. Med.,* 14(1):34.

Porra, L., Monfraix, S., Berruyer, G., Le Duc, G., Nemoz, C., Thomlinson, W., Suortti, P., Sovijärvi, A. & Bayat, S. (2004). Effect of tidal volume on distribution of ventilation assessed by synchrotron radiation CT in rabbit. *Journal of Applied Physiology,* 96(5):1899-1908.

Porra, L. (2006). Lung structure and function studied by synchrotron radiation. *Report series in physics*, University of Helsinki, 128.

Porra, L., Bayat, S., Strengell, S., Suhonen, H., Sovijärvi, A. R. A., Suortti, P. (2009). *American Thoracic Society international conference 15-20.5.2009, San Diego, USA. Presentation* [Publication Page: A1061].

Rahmim, A., Zaidi, H. (2008). PET versus SPECT: strengths, limitations and challenges. *Nucl. Med. Commun.,* 29(3):193-207. Review.

Ramchandani R, Shen X, Elmsley CL, Ambrosius WT, Gunst SJ, Tepper RS. (2000). Differences in airway structure in immature and mature rabbits. *J. Appl. Physiol. (1985)*, 89(4):1310-6.

Renier, M., Fiedler, S., Nemoz, C., Gonzalez, H., Berruyer, G., Bravin, A. (2005). A mechanical chopper with continuously adjustable duty cycle for a wide X-ray beam. *Nucl. Instrum. Methods Phys. Res.,* A548 111-115.

Roessl, E., Proksa, R. (2007). K-edge imaging in x-ray computed tomography using multi-bin photon counting detectors. *Phys. Med. Biol.,* 52:4679–4696.

Roffel, A. F., Elzinga, C. R., Zaagsma, J. (1990). Muscarinic M3 receptors mediate contraction of human central and peripheral airway smooth muscle. *Pulm. Pharmacol.* 3(1):47-51.

Rose, A. (1973) Vision - Human and Electronic (*New York, NY: Plenum*).

Rubenstein, E., Hofstadter, R., Zeman, H.D., Thompson, A.C., Otis, J.N., Brown, G.S., Giacomini, J.C., Gordon, H.J., Kernoff, R.S., Harrison, D.C., and Thomlinson, W. (1986) Transvenous coronary angiography in humans using synchrotron radiation. *Proc. Natl. Acad. Sci. U S A.,* 83(24):9724-8.

Samei, E., Flynn, M. J., Reimann, D. A. (1998). A method for measuring the presampled MTF of digital radiographic systems using an edge test device. *Med. Phys.,* 25: 102-113.

Sánchez-Crespo, A., Andreo, P., Larsson, S.A. (2004). Positron flight in human tissues and its influence on PET image spatial resolution. *Eur. J. Nucl. Med. Mol. Imaging*., 31:44–51.

Santyr, G. E., Couch, M. J., Lam, W. W., Ouriadov, A., Drangova, M., McCormack, D. G., Holdsworth, D. W. (2011). Comparison of hyperpolarized (3)He MRI with Xe-enhanced computed tomography imaging forventilation mapping of rat lung. *NMR Biomed.* 24(9):1073-80.

Sarnelli, A., Nemoz, C., Elleaume, H., Estève, F., Bertrand, B., Bravin, A. (2005). Quantitative analysis of synchrotron radiation intravenous angiographic images. *Phys. Med. Biol.,* 50(4) 725-40.

Simon, B. A., Marcucci, C., Fung, M., Lele, S. R. (1998). Parameter estimation and confidence intervals for Xe-CT ventilation studies: a Monte Carlo approach. *J. Appl. Physiol. (1985),* 84(2):709-16.

Sovijärvi, A.R., Pöyhönen, L., Kellomäki, L., Muittari, A. (1982). Effects of acute and long-term bronchodilator treatment on regional lung function in asthma assessed with krypton-81m and technetium-99m-labelled macroaggregates. *Thorax,* 37(7):516-20.

Sovijärvi, A.R., Pajunen, J., Turjanmaa, V., Uusitalo, A. (1986). Reference values of regional ventilation, lung volumes and perfusion assessed by using an automated multidetector 133-Xe radiospirometer. *Ann. Clin. Res.,* 18(3):160-6.

Suhonen H, Porra L, Bayat S, Sovijärvi AR, Suortti P. (2008). Simultaneous in vivo synchrotron radiation computed tomography of regional ventilation and blood volume in rabbit lung using combined K-edge and temporal subtraction. *Phys. Med. Biol.,* 53(3):775-91.

Suortti, P., Thomlinson, W., Chapman, D., Gmür, N., Siddons, D. P., Schulze, C. (1993). A single crystal bent Laue monochromator for coronary angiography. *Nucl. Instrum. Methods,* A336:304-309.

Suortti, P., Fiedler, S., Bravin, A., Brochard, T., Mattenet, M., Renier, M., Spanne, P., Thomlinson, W., Charvet, A. M., Elleaume, H., Schulze-Briese, C., Thompson, A. C. (2000). Fixed-exit monochromator for computed tomography with synchrotron radiation at energies 18-90 keV *J. Synchrotron. Radiat.,* 7(5):340-7.

Suortti, P., Thomlinson, W. (2003). Medical applications of synchrotron radiation. *Phys. Med. Biol.* 48(13) R1-35. Review.

Suzuki, A., Suzuki, M. N. (1978). Use of a pencil-shaped ionization chamber for measurement of exposure resulting from a computed tomography scan. *Med. Phys.,* 5(6):536-9.

Tai, Y.C., Laforest, R. (2005). Instrumentation aspects of animal PET. *Annu. Rev. Biomed. Eng.,* 7:255-85. Review.

Thien, F. (2013). Measuring and imaging small airways dysfunction in asthma. *Asia Pac. Allergy.,* 3(4):224-30.

Thiesse, J., Namati, E., Sieren, J. C., Smith, A. R., Reinhardt, J. M., Hoffman, E. A., McLennan, G. (2010). Lung structure phenotype variation in inbred mouse strains revealed through in vivo micro-CT imaging. *J. Appl. Physiol. (1985),* 109(6):1960-8.

Thomlinson, W. (1996). Proceedings of the International School of Physics `Enrico Fermi', Course CXXVIII, edited by E. Burattini & A. Balerna, *Amsterdam: IOS Press.*, 127-153.

Thompson, A.C., Llacer, J., Campbell Finman L., Hughes, E.B., Otis, J.N., Wilson, S., Zeman, H.D. (1984). Computed tomography using synchrotron radiation. *Nuclear Instruments and Methods in Physics Research,* 01.

Tzeng, Y.S., Hoffman, E., Cook-Granroth, J., Gereige, J., Mansour, J., Washko, G., Cho, M., Stepp, E., Lutchen, K., Albert, M.. (2008). Investigation of hyperpolarized 3He magnetic resonance imaging utility in examining human airway diameter behavior in asthma through comparison with high-resolution computed tomography. *Acad. Radiol.,* 15(6):799-808.

Tzeng, Y. S., Lutchen, K., Albert, M. (2009). The difference in ventilation heterogeneity between asthmatic and healthy subjects quantified using hyperpolarized 3He MRI. *J. Appl. Physiol.*, 106: 813–22.

Venegas, J. G., Winkler, T., Musch, G. Vidal Melo, M. F., Layfield, D., Tgavalekos, N., Fischman, A.J., Callahan, R.J., Bellani, G., Harris, R.S. (2005). Self-organized patchiness in asthma as a prelude to catastrophic shifts. *Nature,* 434: 777–82.

Vieira, S. R., Puybasset, L., Lu, Q., Richecoeur, J., Cluzel, P., Coriat, P., Rouby, J.J. (1999). A scanographic assessment of pulmonary mor- phology in acute lung injury. Significance of the lower inflec- tion point detected on the lung pressure-volume curve. *Am. J. Respir. Crit. Care Med.,* 159(5 Pt 1):1612-23.

WHO, World Health Organization. (2007). Global surveillance, prevention and control of chronic respiratory diseases: a comprehensive approach, 2007.

Wohlsen, A., Martin, C., Vollmer, E., Branscheid, D., Magnussen, H., Becker, W.M., Lepp, U., Uhlig, S. (2003). The early allergic response in small airways of human precision-cut lung slices. *Eur. Respir. J.,* 21(6):1024-32.

Yamada, Y., Jinzaki, M., Hosokawa, T., Tanami, Y., Sugiura, H., Abe, T., Kuribayashi, S. (2012). Dose reduction in chest CT: comparison of the adaptive iterative dose reduction 3D, adaptive iterative dose reduction, and filtered back projection reconstruction techniques. *Eur. J. Radiol.* 81(12):4185-95.

Zhang, G., Dilling, T.J., Stevens, C.W., Forster, K.M. (2008). Functional lung imaging in thoracic cancer radiotherapy. *Cancer Control*, 15(2):112-9. Review.